DOI:10.15774/PPKE.ITK.2015.003

Fast three-dimensional two-photon scanning methods for studying neuronal physiology on cellular and network level

Doctoral dissertation

Gergely Katona

Supervisor:

Dr. Balázs Rózsa PhD.

Pázmány Péter Catholic University
Faculty of Information Technology
Multidisciplinary Doctoral School of Sciences and Technology

Budapest, 2014

DOI:10.15774/PPKE.ITK.2015.003

DOI:10.15774/PPKE.ITK.2015.003

DOI:10.15774/PPKE.ITK.2015.003

DOI:10.15774/PPKE.ITK.2015.003

ACKNOWLEDGEMENT

I would like to thank my friend and scientific advisor Dr. Balázs Rózsa for guiding and supporting me over the years.

Many thanks go out to co-authors and my other colleagues in our research group for their friendship and/or for the knowledge and the amazing times we spent together: *Alexandra Bojdán, András Vági, Attila Kaszás, Balázs Chiovini, Botond Roska, Dániel Hillier, Dénes Pálfi, Dorina Gündisch, Ferenc Csikor, Ferenc Erdélyi, Gábor Szabó, Gábor Tamás, Gergely Szalay, Gergely Turi, Klaudia Sptizer, Linda Judák, Máté Veress, Norbert Hájos, Pál Maák, Patricia Varjú, Szabolcs Káli, Zoltán Szadai,*

I am grateful to Prof. Tamás Roska, Prof. Péter Szolgay and Prof. Sylvester E. Vizi for paving the way to carry out my research at the University and at the Institute of Experimental Medicine, HAS.

This work was supported by the grants OM-00131/2007, OM-00132/2007, GOP-1.1.1-08/1-2008-0085, NK 72959, Grant of Hungarian Academy of Sciences, French grant (TÉT_0389), Swiss-Hungarian grant SH/7/2/8, KMR_0214, FP7-ICT-2011-C 323945.

Last and most importantly, I cannot really express the level of gratitude to my Family, my wife Viki, and my sons Dani and Ádám, who were missing me during many night shifts and who were always there for me to share the good times and the hard ones as well.

In phrasing my thesis I used text from my publications (Katona et al., 2011; Katona et al., 2012) and in the introduction I also used some words of W. Denk, father of two-photon microscopy (Denk and Svoboda, 1997).

DOI:10.15774/PPKE.ITK.2015.003

CONTENTS

DOI:10.15774/PPKE.ITK.2015.003

DOI:10.15774/PPKE.ITK.2015.003

LIST OF FIGURES

DOI:10.15774/PPKE.ITK.2015.003

DOI:10.15774/PPKE.ITK.2015.003

ABBREVIATIONS

2D – two dimensional

3D – three dimensional

AO – acousto-optic

AP – action potential

bAP – backpropagating action potential

FOV – field of view

FWHM – full width at half maximum

NCX1 – Na^{+}/Ca^{2+} exchanger

NMDA – N-methyl-D-aspartate

PSF – point spread function

PMT – photomultiplier

ROI – region of interest

SEM – standard error of the mean

SNR – signal-to-noise ratio

DOI:10.15774/PPKE.ITK.2015.003

1 INTRODUCTION

How does the brain work? This ancient question was in the focus of many clever minds in the past, from Aristotle through Szentágothai all the way to recent high profile laboratories. However, with the development of technology new approaches could emerge. Aristotle could only rely on thinking and deduction (Gross, 1995), while with the invention of Golgi (Golgi, 1873), the novel era of neuroscience could emerge focusing on the morphology and structure of the brain. This detailed anatomical knowledge is accompanied in the recent decades with the emergence of new investigation technologies fuelling a new boom in the functional knowledge about our initial question. The revolution in this field is best underlined with the fact that in 2014 two Nobel prizes have been awarded to achievements related to functional imaging. Stefan Hell and his colleagues were awarded Nobel Prize in Chemistry because their pioneering work on superresolution fluorescent technology, STED (stimulated emission depletion), with which it is possible to study cellular processes at nanometer resolution (Hell and Wichmann, 1994; Betzig et al., 2006). Nobel prize In Physiology and Medicine was awarded for discoveries of cells that constitute a positioning system in the brain (Hafting et al., 2005). Through the work of John O'Keefe and the Moser couple this positioning system became one of the most studied high level complex network function. They used electrode arrays implanted in the brain of the animals, but we hope two-photon imaging will be able to complement these functional studies as my thesis is ultimately dedicated to make two-photon scanning also capable of neuronal network level investigations.

The systematic understanding of brain function requires methods that allow neuronal activity to be recorded at different spatial scales in three dimensions (3D) at a high temporal resolution (ideally over kHz). At single neuron level activity is differentially distributed in space and time across the dendritic and axonal segments (Rozsa et al., 2004; Johnston and Narayanan, 2008; Losonczy et al., 2008; Rozsa et al., 2008; Spruston, 2008; Katona et al., 2011). Therefore, in order to understand neuronal signal integration, activity should be simultaneously recorded at many (at least 10-100) spatial locations within the dendritic and axonal tree of a single neuron. At neuronal circuit level, closely spaced neurons can have

DOI:10.15774/PPKE.ITK.2015.003

vastly different activity patterns (Ohki et al., 2005); on the other hand, widely separated cells may belong to the same functional circuit, influencing each other via long axonal processes. Therefore, recording techniques are required that collect information near-simultaneously (ideally measurement at all locations within a millisecond) from many cells of a neuronal population situated in an extensive volume of tissue (ideally over a cubic millimeter). Moreover, measurement should be possible on the timescales of the dendritic integration and regenerative spike propagation (Ariav et al., 2003), i.e., with sub-millisecond temporal resolution. One last aspect is that these measurements should be performed on neurons or neuronal networks which are as intact as possible, where neurons are embedded in their original tissue. This poses a challenge: cellular precision must be retained in acute brain preparations where the tissue is at least 100 µm thick or, for *in vivo* experiments, through millimeters of brain material.

Light microscopy is important in biological research because it enables living tissue to be observed and studied at a relatively high spatial resolution. This resolution is limited by the wavelength of light and even with superresolution technologies (Hell and Wichmann, 1994; Betzig et al., 2006) does not rival that of electron microscopy. However electron microscopy is limited in its ability to observe living specimens (Danilatos, 1991). Other vital imaging technologies, such as MRT (magnetic resonance tomography), PET (positron emission tomography) or X-rays, can neither resolve subcellular structures nor provide high temporal resolution nor the exquisite molecular selectivity that would allow single molecules to be detected against a background of billions of others (Kerr and Denk, 2008; Kherlopian et al., 2008).

Light microscopy inside living tissues is hampered by the degradation of resolution and contrast, caused by absorption and light scattering, which is due to refractive index inhomogeneities present to a varying degree in every tissue. Deeper within the tissue, images become more degraded and high-resolution imaging eventually becomes impossible. A major step toward overcoming this problem was the invention of confocal microscopy (Amos et al., 1987; Minsky, 1988). In a confocal microscope, the illumination light is focused on a diffraction-limited spot, and this excites the sample along two cones close to the aimed focal point. Then, using the same objective, the emitted signal photons are focused onto a detector pinhole that rejects all light emitted outside of the focal point.

DOI:10.15774/PPKE.ITK.2015.003

The main drawback of confocal microscopy is its wasteful use of both excitation and emission. On the one hand, absorption occurs throughout the specimen, but information is obtained only from a small volume around the focal point. On the other hand, light emitted from the focal point is also rejected by the pinhole if it is scattered by the tissue; this means that tissue scattering has a significant impact on the signal-to-noise ratio (SNR) of the images. This is a major problem particularly in vital fluorescence microscopy, where the limiting factors are usually either the photochemical destruction of the fluorophore (photobleaching) or the photodynamic damage to the specimen (photodamage). In confocal microscopy, only those ballistic photons that are not scattered on their way out of the tissue contribute to the signal: scattered photons, often the majority, are rejected by the detector aperture, limiting depth penetration using this technique to about 50-80 µm in brain tissue. Excitation needs to be increased in order to compensate for this signal loss, and this further exacerbates photobleaching and photodamage. All of these problems are also found in many other, so-called single-photon excitation technologies, among them spinning-disc confocal microscopy (Petráň et al., 1968) and light sheet microscopy (Tomer et al., 2012). Fortunately, these problems can be handled by using laser scanning microscopy in combination with two-photon excitation (Denk et al., 1990; Denk and Svoboda, 1997).

The concept of two-photon excitation is based on the idea that two photons of low energy can be combined in the same quantum event, resulting in the emission of a fluorescence photon at a higher energy than either one of the two excitatory photons. Although the probability of such absorption is extremely low, its cross section is proportional to the square of the photon flux, making it possible to counterbalance this low initial cross section by using extremely high photon fluxes. Two-photon absorption is often called nonlinear because the absorption rate is dependent on a higher-than-first-power light intensity. Such high fluxes are only present in the focus of a high numerical aperture lens illuminated by a strong, pulsed near-infrared laser.

The possibility of absorbing more than one photon during a single quantum event had been predicted more than 60 years ago (Goeppert-Mayer, 1931), but it was only confirmed experimentally after the invention of the lasers. Mode-locked lasers with a pulse duration below 1 ps and repetition rates of about 100 MHz made two-photon laser scanning microscopy feasible in practice (Denk et al., 1990).

DOI:10.15774/PPKE.ITK.2015.003

Because the two-photon effect depend on the square of the intensity density, pulsing the laser source increases the average two-photon excitation rate compared to continuous-wave (CW) operation at the same average power. A typical Ti:sapphire laser has roughly 100 fs pulse width and 10 ns pulse repetition rate, thus it boosts the two-photon excitation rate by 100,000-fold. For the same reason, the quadratic dependence of the absorption rate on the light intensity gives two-photon microscopy its optical sectioning property because fluorescence is only generated in the vicinity of the geometrical focus where the light intensity is high. While scanning the laser focus in both lateral directions (*x* and *y*), fluorescence excitation is limited to the focal plane. No detector pinhole is necessary since – in most cases – no fluorescence is generated outside the focal volume, and all fluorescence photons, whether leaving the sample on scattered or ballistic trajectories, constitute useful signal.

The combination of low phototoxicity enabled by the single point excitation and the efficient use of fluorescence – even scattered – makes single-point two-photon microscopy a unique tool for observing function deep within the tissue; resolving small structures deeper than one millimeter in the brain (Theer et al., 2003; Helmchen and Denk, 2005; Kobat et al., 2011). Its main drawback, however, is speed when compared to camera-based approaches where, instead of the ‘single-channel’ photomultipliers (PMTs), information can potentially be collected from millions of camera pixels simultaneously.

There are several approaches to using multi-site two-photon stimulation in combination with a camera-based detection algorithm to overcome the limitation of single-point illumination.

The simplest of these technologies is multi-beam two-photon microscopy (Niesner et al., 2007), where a string of focal spots are generated by breaking the laser beam into parallel beamlets. This causes parallel fluorescent excitation at multiple sites which are scanned to illuminate the entire focal plane. Fluorescence is detected by a high-resolution camera after imaging the focal plane onto its sensor chip. This approach makes it possible to image with a higher frame rate than with a scanned single-beam two-photon microscope, but it has one main drawback: imaging fluorescence onto the camera is sensitive to tissue scattering. As a result, this technology has about half of the penetration depth of single-point two-photon

DOI:10.15774/PPKE.ITK.2015.003

microscopy and this – especially in the case of *in vivo* investigations – seriously limits its biological usability.

Recent camera-based approaches can also resolve the 3D structure of a sample by using a special light shaping microlens array (Prevedel et al., 2014) or phase mask (Quirin et al., 2014) in front of the camera combined with extended depth of field (Quirin et al., 2013) or holographic (Quirin et al., 2014) illumination. Depth information is obtained from the camera images by a computational reverse transformation which causes two major limitations. First, there is a strict limit to the number and arrangement of the regions of interest (ROIs) as they should not overlap much on the detector surface. Typically, ROIs situated at the same place but at different depths are imaged to mostly overlapping profiles on the detector surface, making it difficult to distinguish between them. Second, the imaging of the emitted light to the camera is – again – sensitive to tissue scattering, causing scattered shapes on the detector surface, challenging the reverse transformation algorithms. For example, Quirin et al., 2014 showed penetration depth of about 190 µm (3x scattering length) which is just enough to reach the first cell layers in mice *in vivo*, and is much less than the depths achievable by single-point two-photon microscopes.

As we have seen, a single-point two-photon microscope can reach deep structures with subcellular resolution, which makes this technology the best available tool for functional studies. However, as only one point might be illuminated at a time, special scanning methods need to be developed to sample the important biological features with enough speed to resolve their functionality. My work detailed in the next sections is dedicated to finding out and implementing such scanning methods, devices, electronics and software, and to perform cellular level biological measurements in acute brain slices and in the brain of living animals. More specifically my main aims were:

- Development of a fast scanning method for a two-photon microscope to sample sparse regions of interests effectively, e.g. to measure multiple compartments of the dendritic tree of neurons within 10 ms. (Chapter 2, Thesis 1)
- Development of a two-photon microscope capable of scanning 3D structures with high speed, e.g. to sample long tortuous dendrites with at least 100 Hz. (Chapter 3, Thesis 2)

DOI:10.15774/PPKE.ITK.2015.003

- Development of a 3D random-access scanning capable two-photon microscope which is able to sample activity from many cells near simultaneously. (Chapter 4, Thesis 3)

DOI:10.15774/PPKE.ITK.2015.003

2 FAST 2D REGION OF INTEREST SCANNING (THESIS 1)

In this chapter I will describe a scanning technology we developed for fast measurement of fluorescence in multiple regions selected in the focal plane. By describing this relatively simple method I will introduce some basic principles we used later in our more complex 3D technologies detailed in chapters 3 and 4.

2.1 The two-photon microscope

In a two-photon microscope (Figure 1) the laser beam used to excite the fluorescent dye is directed into the microscope via an epifluorescent light path. The excitation light is passed through a dichroic mirror to the microscope objective and is focused in the specimen. Two-photon induced fluorescence is generated only at the focal spot. Images are constructed by (raster) scanning the fluorescent volume by using a galvanometer-driven *x*–*y* scanner. The emission signal is collected by the same objective (and alternatively through the condenser) and reflected by the dichroic mirror to the detector. An additional barrier filter is needed to further attenuate the scattered excitation light. High-sensitivity detectors and electronics are used to ensure maximal detection efficiency.

The excitation light is usually a tunable mode-locked Ti:sapphire laser working at a wavelength set between 700 and 1000 nm. Fluorescent staining molecules having emission in the visible regime (500-600 nm) are used, while the dichroic mirror separates excitation and emission at about 700 nm. Optical resolution is limited by the Abbe law (modified for two photon excitation) thus it depends on the excitation wavelength and the numerical aperture of the focusing. Usually large working distance (1-3 mm) water immersion objectives are used having numerical aperture about 1, thus the lateral optical resolution is expected to be around 350-500 nm.

Galvanometers are commanded to perform raster scanning to form images and as the current commercially available scanners have a maximal driving frequency of about 2 kHz, full field images (512 x 512 pixels) can be obtained maximally at 4 frames per second speed.

DOI:10.15774/PPKE.ITK.2015.003

We constructed a two photon microscope hosting all our improvements detailed below, for details see 2.6 Materials and methods section.

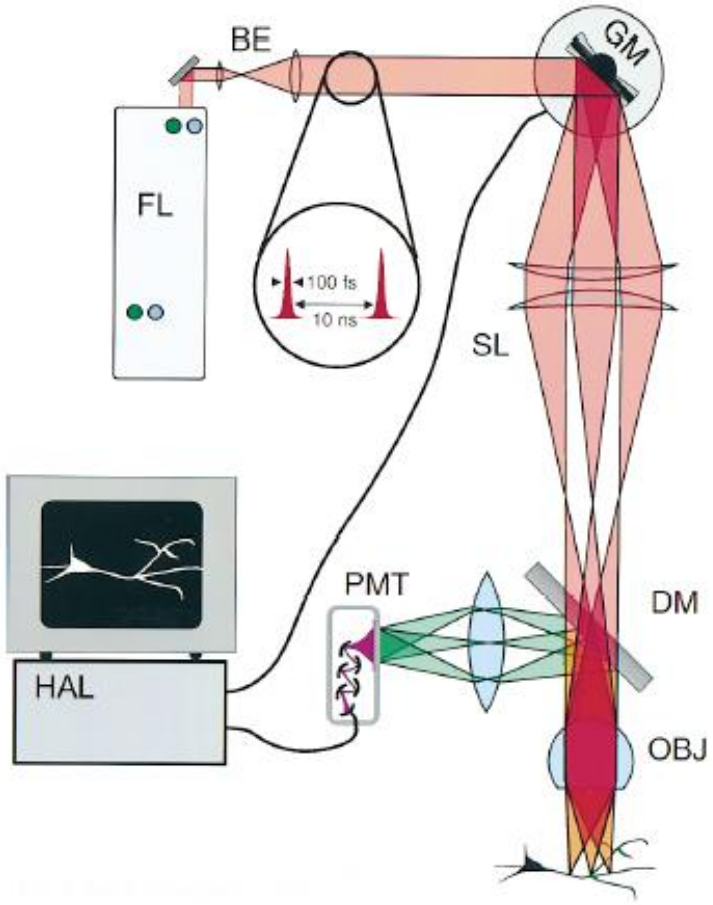

Figure 1 Schematics of a two-photon microscope

The excitation light, a train of femtosecond pulses from the mode-locked (FL) laser, passes the beam expander (BE), a pair of galvanometer scanning mirrors (GM, only one axis shown), the scan-lens (SL, essentially a low magnification eyepiece), intermediate optics inside the microscope (not shown), the objective lens (OBJ), and comes to a diffraction-limited focus inside the specimen. Some fraction of the 2-photon excited fluorescence passes back through the objective (detection of light entering the condenser or coming off to the side is possible as well) and is deflected by a dichroic mirror (DM) through a filter (blocking excitation light, not shown) into the photomultiplier detector (PMT). A computer (HAL) controls the scanners and synchronously records the signal from the PMT. Figure adopted from Denk and Svoboda, 1997.

DOI:10.15774/PPKE.ITK.2015.003

2.2 Why region of interest scanning?

In two-photon microscopy images are traditionally obtained. These images are formed by measuring the fluorescence intensities in all pixels, moving the focal spot line-by-line; therefore it is also called raster scanning. An ideal device to capture full images with high frame rate is the so called, resonant-galvo system. Here the mirror deflecting laser light in the x direction is mounted on a resonant scanner which is actually made of a flexible torsion mechanics and an electromotor. The motor is driven by a feedback loop making the system oscillate very fast (8 kHz in typical commercially available devices) resulting in 31 frames captured per second (512 x 512 pixels, full field) (Fan et al., 1999; Jia et al., 2010).

To record neuronal signaling and action potentials (APs) however, much larger repetition rates are necessary (ideally near kHz). To reach this goal we should give up recording entire images and instead of sampling all pixels in images we need to scan repetitively only the regions containing information for the experimenter (region of interest - ROIs).

As we measure a low number of photons (λ), the mean signal (μ) captured from a ROI and its variance (σ) follow Poisson distribution:

Equation 1. $$SNR = \frac{\mu}{\sqrt{\sigma}} = \frac{\lambda}{\sqrt{\lambda}} = \sqrt{\lambda}$$

Thus SNR is predominantly determined by the total number of photons collected from a structure within a unit time. On the other hand, the total number of photons can be written as:

Equation 2. $$\lambda = \eta \cdot \varphi \cdot \tau$$

where η is the systems total efficiency for detecting an emitted photon (constant), φ is the emitted photon flux, and τ is the time spent on the ROI. Because increasing excitation in living samples quickly results in photobleaching and photodamage, we cannot increase φ above a certain level (determined experimentally for each sample preparation) so one can increase SNR only by increasing the time fraction spent on the ROIs.

Giving up scanning images and scanning strictly the ROIs increases the time fraction the scanner spends on the ROIs and by this ultimately increases the SNR of the information collected from the ROIs. When we select scanning lines to cover the ROIs instead of raster

DOI:10.15774/PPKE.ITK.2015.003

scanning, total number of photons sampled from the ROI will be increased with the ratio of the time fraction spent on the ROIs during raster scanning. This is proportional to the raster scanned field of view versus the ROI area.

Equation 3.

$$(\text{SNR gain}) = \sqrt{\text{increase in the total number of photons}} = \sqrt{\frac{total\ image\ area}{area\ illuminated\ by\ the\ scan\ line}}$$

This means that if the ROIs are small and dispersed in the (2D) field of view (FOV) – which is the usual case – one can increase SNR significantly by repetitively scanning only the information containing areas using line-scans instead of raster scanning the full (mostly not labeled) areas. The quantity of the SNR gain is dependent on the shape and extent of the ROIs, thus the geometry to be scanned.

2.3 Multiple Line Scanning

Earlier realizations could perform line-scanning only on single, straight horizontal lines which were often not matching the shape of the ROIs (Rozsa et al., 2004). We developed a system (Lorincz et al., 2007; Rozsa et al., 2008) using galvanomotor-based scanning mirrors. These scanner motors are driven (by an appropriate closed loop driving electronics) so that their absolute position can be specified by the input analog voltage signals (see 2.6 Materials and methods). I implemented in the software that the desired regions can be drawn onto the previously made raster scanned background image. Measurement line can be constituted of multiple straight or curved line segments to cover various combinations of ROIs. These line segments can be scanned with constant speed, while intermediate sections are jumped over within 60-100 µs, using a spline interpolated path (Figure 2). We named this technology Multiple Line Scanning. Using high speed galvomotors and high performance driving electronics complex line-scans consisting of a dozen line segments can be typically performed with 100-200 Hz repetition rate, but on small straight line segments this can be tuned up to about 2 kHz.

Figure 2 shows a dendritic segment where the activity of multiple spines and their parent dendritic segment can be recorded simultaneously with Multiple Lines Scanning, resolving

DOI:10.15774/PPKE.ITK.2015.003

individual postsynaptic events and the diffusion of Ca^{2+} between compartments. Quantitatively the SNR gain according to Equation 3 in the case on Figure 2 (image area is 16 µm x 7 µm, ROI area is 20 µm x 0,5 µm which latter is the diameter of the PSF) results in a factor of 3,3. Another common situation is if we want to measure a 14 µm long dendritic portion caught diagonally in the field of view. With raster scanning we would need to scan a 10 by 10 µm image, thus the SNR gain according to Equation 3 (image area is 10 µm x 10 µm, ROI area is 14 µm x 0,5 µm) results in a factor of 3,8. Evaluating other likely situations of imaging dendrites, we can say that the SNR gain is approximately 3-4. Theoretically the lower extreme is 1 in the case of rectangular ROIs fully filling the raster scan; an upper extreme is if the ROI is thin, diagonal and spans the entire FOV (approximately 600 µm with a 20x objective), in this case SNR gain is 29. As raster scanning the full field of view (512 x 512 pixels; using galvanometer based scanners) is possible with only 4 Hz, we can say that the repetition rate increase is again depending on the shape and extent of the ROI, but it is between 1 and 512.

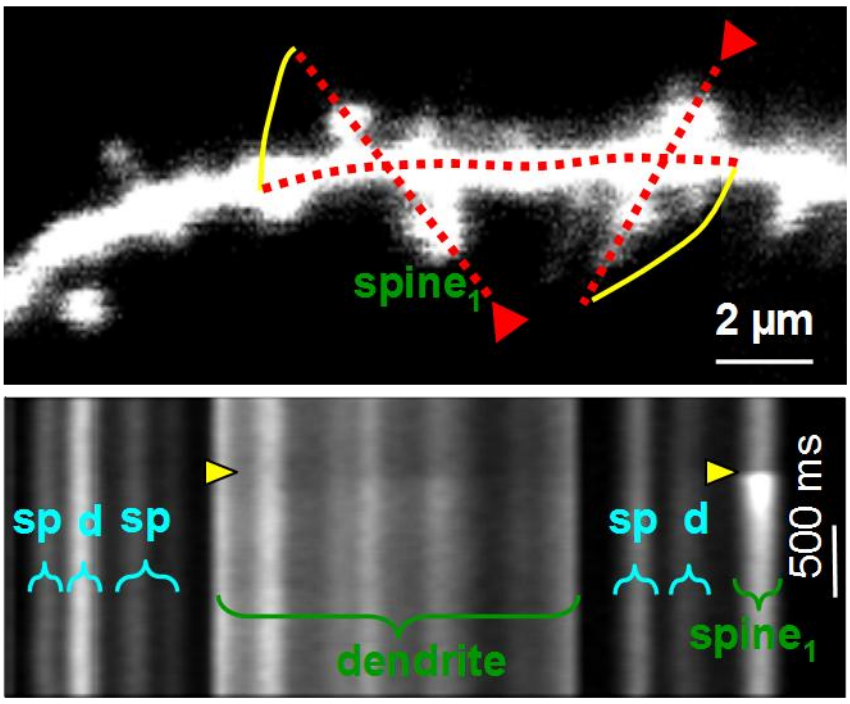

Figure 2 Multiple Line Scan covering multiple ROIs.

(Top) Multiple Line Scan drawn on a tortuous dendritic segment: two line segments cross dendritic spines and the dendrite, while the third is selected to follow the dendritic shaft linking them. (Bottom) Raw fluorescence image. Horizontal axis is space "along the line". $Spine_1$ receives a massive synaptic input at the time indicated by yellow triangles. As a result of Ca^{2+} diffusing

DOI:10.15774/PPKE.ITK.2015.003

out of the spine neck a smaller, dispersed Ca^{2+} transient can also be seen in the dendritic shaft. (Lorincz et al., 2007)

2.4 Using line-scans to investigate dendritic Ca^{2+} dynamics

To prove the method is beneficial in biological measurements, I describe here a study we performed. Using the new method and the prototype we built we studied the role of Na^{+}/Ca^{2+} exchanger (NCX1) on dendritic shafts (Lorincz et al., 2007).

In this study a major benefit of using the Multiple Line Scanning method was that by simultaneously scanning neighboring spine-dendrite pairs (Figure 2) we were easily able to isolate the cases where only single spines were activated. We used extracellular synaptic stimulation where a glass pipette is placed near (5-10 μm) the investigated dendritic segment and we tried to stimulate unlabeled axons converging onto the investigated dendrite by introducing current pulses to the pipette (see 2.6 Materials and methods). Even with carefully chosen location and current level, it is hard to selectively activate single synaptic inputs. Activation of the neighboring spines can lead to an increased Ca^{2+} influx as a result of the removal of the magnesium block of NMDA (N-methyl-D-aspartate) channel and/or the opening of voltage gated Ca^{2+} channels. Without the monitoring of neighboring synaptic activity, it cannot be excluded that the larger, previously reported Ca^{2+} signals (Mainen et al., 1999; Kovalchuk et al., 2000) are the consequence of the activation of neighboring synaptic inputs. Using our Multiple Line Scanning method we could rule out these events and study the action of NCX1s in those biologically relevant cases too, where only one synapse was activated at a time (**Hiba! A hivatkozási forrás nem található.**a). This results in smaller Ca^{2+} signals restricted to spines and are comparable to more recent experiments, where single synaptic inputs elicited Ca^{2+} signals well compartmentalized to spines without spreading to neighboring shafts (Yuste et al., 2000).

Benzamil selectively blocks Na^{+}/Ca^{2+} exchange in small concentration (30 μM) resulting in a modest effect on Ca^{2+} transients. With the improved SNR of Multiple Line Scanning we were able to significantly resolve these subtle differences in Ca^{2+} transients and therefore could show NCX1 activity in dendritic shafts and spines during repeated stimulation of single synapses (**Hiba! A hivatkozási forrás nem található.**b).

DOI:10.15774/PPKE.ITK.2015.003

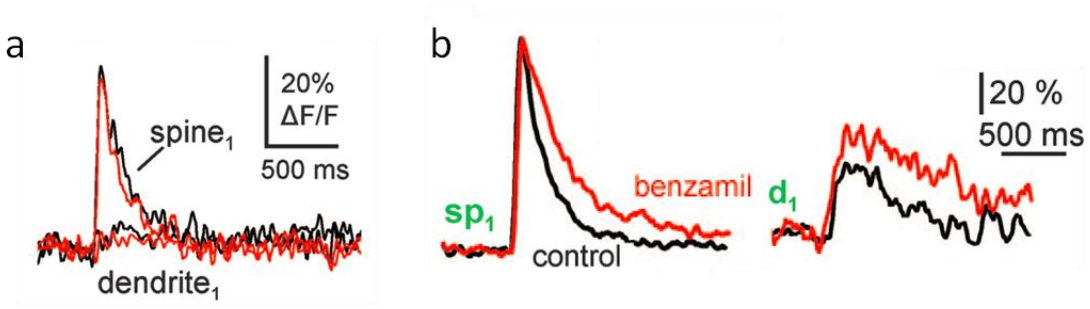

Figure 3 The effect of benzamil on dendritic Ca^{2+} transients.

*(**a**) NCX1 activity does not shape Ca^{2+} transients compartmentalized to dendritic spines during single synaptic stimulation. Example average responses in the dendrite and spine in the presence (red) and absence (black) of 30 µM benzamil. (**b**) NCX1 activity does shape Ca^{2+} transients in dendritic shafts and spines during repeated stimulation of single synapses. Synaptic stimulation was elicited by seven consecutive stimuli delivered at 200 Hz. Normalized Ca^{2+} transients in a spine (Left) and parent dendrite (Right) in control conditions (black traces) and in the presence of benzamil (red traces). Traces are averages of four responses. (Lorincz et al., 2007)*

We also took advantage of Multiple Line Scanning to record multiple locations with good SNR in other studies, where we studied the attenuation of backpropagating action potentials (bAPs) in interneuron dendrites (Rozsa et al., 2008; Chiovini et al., 2010).

2.5 Discussion

Multiple Line Scanning is a versatile tool which allows Ca^{2+} imaging in neuroscience on subcellular components i.e. on dendritic structures, and is capable of simultaneously recording multiple cellular processes or multiple somata, but for example it also allows blood flow measurements in capillaries. Its main benefit is increased repetition rate and SNR of the signal collection from the ROIs selected in the focal plane. The repetition rate increase compared to classical raster scanning is between 1 and 512, typically 10-100. The increase of SNR is between 1 and 29, typically 3-4. On the top of this, the technology can also be used for photostimulation with single scan head: for two-photon uncaging (Katona et al., 2011), optogenetical activation, and FRAP (fluorescence recovery after photobleaching) measurements.

DOI:10.15774/PPKE.ITK.2015.003

2.6 Materials and methods

Electrophysiology. Pyramidal cells in the CA1 subfield of the hippocampus were visualized under 900-nm infrared differential interference contrast (DIC; 900 nm; Olympus, Budapest, Hungary). Electrodes (6–9 MΩ) were filled with 125 mM potassium gluconate, 20 mM KCl, 10 mM Hepes, 10 mM Di-Tris-salt phosphocreatine, 0.3 mM Na-GTP, 4 mM Mg-ATP, 10 mM NaCl, and 60 μM Oregon green BAPTA-1. Recordings were made at 32°C by using a MultiClamp 700B Amplifier (Axon Instruments, Foster City, CA). Cells with a resting membrane potential more negative than 65 mV were accepted. Data acquisition was performed by using pClamp8 (Axon Instruments) and a MATLAB program written in our laboratory. We used 6- to 9-MΩ patch electrodes filled with ACSF (artificial cerebrospinal fluid) for synaptic stimulation.

Two-photon imaging system. Imaging was performed by using a two-photon laser scanning system built in our laboratory. Excitation was provided by a titanium-sapphire laser (R&D Kft., Budapest, Hungary; Millennia Pro, SpectraPhysics, Fremont, CA) providing 100-fs pulses at 80 MHz at a wavelength of 805-810 nm. Focal scanning was achieved by using galvanometric scanners (VM-500; GSI Lumonics, Unterschleissheim, Germany) with a digital servo tuned for high-speed random scanning (Digital Servo; GSI Lumonics). Fluorescence was detected in the external, whole-field detection mode with photomultiplier tubes (R3896; Hamamatsu, Herrsching, Germany). Colored glass filters (BG39; CVI Technical Optics) and dichroic mirrors (750DCSX, 750DCXXR; Chroma Technology, Brattleboro, VT) were used to separate emitted fluorescence from excitation light. Position of the detectors and appropriate lenses and condenser (U-UCD8, NA = 1.4; Olympus, Budapest, Hungary) was optimized for best fluorescence collection, and the intensity of excitation laser light was also always maintained at the minimum required to attain sufficient SNR to minimize photodamage. We developed electronics and a function generator (computer card) to drive the scanner motor-directed light with high accuracy (<300 nm) along arbitrary curves at high scanning speed (>1 kHz) in the focal plane. Data recording started 20–30 min after break-in. At the end of each experiment, a series of images across the depth of the volume encompassing the imaged neuron was taken. Measurement control, real time data acquisition, and analysis were performed with a MATLAB program developed in our laboratory. Fluorescence traces are expressed as relative fluorescence changes [$\Delta F/F = (F-$

DOI:10.15774/PPKE.ITK.2015.003

$F_0)/F_0$], where F_0 is the background-corrected prestimulus fluorescence. If not indicated otherwise, data are presented as means ± SEM. To get the amplitude and decay of the transients, three sweeps were averaged before and after the perfusion of benzamil at high stimulus intensities.

2.7 Thesis

***Thesis 1**: I developed a new method to image dendrites; by limiting the measurements only to the functionally investigated neuronal locations increased speed and signal-to-noise ratio of the measurements significantly.*

Publication related to the thesis: Lorincz et al., 2007, Rozsa et al., 2008; Chiovini et al., 2010.

In two-photon microscopy the scanning is traditionally used to form images. Images are formed by measuring the fluorescence intensities in all pixels, moving the focal spot line-by-line. To record neuronal signaling and action potentials we should give up recording entire images and instead of sampling all pixels we need to scan repetitively only the regions containing interesting information for the experimenter (ROIs). This can be achieved by using galvanometer based scanning mirrors controlled by analog voltage signals boosting repetition speed to the 100 Hz - 1 kHz rate. Scanning only the interesting parts not just increases repetition speed of the measurement at a given ROI, but also increases signal-to-noise ratio (SNR) of the measured fluorescence signals, typically by a factor of 3-4. The higher the ratio of the area of the FOV to the area of the ROIs the larger the possible SNR gain is.

We developed a complex line-scanning method called Multiple Lines Scanning (Lorincz et al., 2007) and built a microscope utilizing it. We were able to use this feature to show Na^+/Ca^{2+} exchanger (NCX1) activity in the case when multiple synaptic inputs arrive in close succession to the same dendritic branch (Lorincz et al., 2007). The major benefit of using the Multiple Line Scanning method was that by simultaneously scanning multiple neighboring spines we were able to isolate the cases where only single spines were activated. We also took advantage of this method to record multiple locations with good SNR in other studies, where we studied the attenuation of backpropagating action potentials (bAPs) in interneuron dendrites (Rozsa et al., 2008; Chiovini et al., 2010).

DOI:10.15774/PPKE.ITK.2015.003

3 PIEZOELECTRIC OBJECTIVE POSITIONER BASED 3D SCANNING (THESIS 2)

Using scanning mirrors to deflect the laser beam enables rapid positioning of the focal point only in the focal plane of the objective. This means that ROIs whose activity we would like to measure with high speed should be within a plane perpendicular to the optical axis; hence we call these scanning methods two dimensional (2D). Biological structures are however rarely planar. Some structures such as hippocampus and the cerebellum gained their popularity because their network functionality can be well understood in slices which are cut parallel to the main connections. Measurement of other structures and even these in *in vivo* conditions asks for methods being able to sample activity in the 3D space. In this chapter I will detail the design of a simple system capable of performing fast 3D scanning.

Traditionally the objective is moved using a step motor driven mechanical arm which enables only slow positioning of the focal plane (Denk et al., 1990) due to the large inertia of the objective and the mechanical arm. Fast *z*-drive by piezo-positioners has been proposed previously (Gobel et al., 2007). In this study, authors moved the objective up and down by forcing the piezo-positioner for a sinusoidal movement. The actual phase shift and amplitude drop was compensated for in the driving signal. In this way, it was possible to resonate the objective with up to 10-20 Hz frequency, which was limited by the deviation of the objective movement from the sinusoidal function above this frequency range. In order to access 3D, Gobel et al performed spiral-scanning by using two galvo mirrors in combination with the sinusoidal objective drive to scan cellular activity within a small volume (250 x 250 x 200 µm) with about 10 Hz repetition rate.

3.1 Roller Coaster Scanning

To achieve faster scanning along a 3D trajectory we coupled to our two-photon microscope (Femto2D, Femtonics) a rapid cylindrically symmetric piezoelectric actuator (Physik Instrumente, Karlsruhe, Germany) with high resonant frequency (~ 1100 Hz without load) and used 100-700 Hz sine wave driving signal (Katona et al., 2011). Speeding up the driving

DOI:10.15774/PPKE.ITK.2015.003

frequency of the piezo-positioner from the earlier described 10 Hz leads not just to a drop in amplitude and change in phase of the sinusoid movement (Gobel et al., 2007), but also resulted in a profound deviation of the position function from the sine wave (Figure 4*A*). We maintained a resonance in the objective movement without servo feedback, whilst measuring the position signal. After 50-100 cycles the movement of the objective reached a steady-state response function z(t) at a mean position (Figure 4*B*). We measured this non-linear z(t) function to generate a drive signal for the *xy* deflection (Figure 4*C*). First, using the z(t) response function, the t_1 time was determined when the focal plane of the objective was at height z_1, $z(t_1)=z_1$, (Figure 4 *Ca* and *Cb*), then at this t_1 time point the *xy* drive signal for the galvanometer scanner was set to (x_1, y_1) to fit the 3D trajectory $f(x_1,y_1,z_1)$ (Figure 4 *Cc*). This process was repeated for the remaining points of the entire 3D trajectory selected for measurement.

We wrote software elements to help the fast orientation in 3D space, the selection of the 3D trajectories according to the *z*-stacks and the optimal utilization of the whole available *z*-scanning range. Namely, after acquisition of a *z*-stack, the recorded image series were used to aid the selection of the 3D path by scrolling through without scanning using the focusing handwheel of the microscope (rotary encoder; M101B, Megatron) for *z* and the computer mouse for *xy* coordinate settings. The selected 3D trajectory was the result of an interpolation algorithm which was based on guide points selected on the image stack of the chosen dendritic region. We named this method Roller Coaster Scanning (Katona et al., 2011) according the similarity in the movement trajectories.

The stability of the 3D trajectory scanning was verified by bleaching 3D curves in a homogeneous fluorescent plastic sample. A z-stack of the fluorescence was taken afterwards, and inverted, representing the time-averaged laser irradiation in the 3D space. When scanning a trajectory with 150 Hz (the same as in Figure 5*A*) shows that the trajectory was followed at high precision in all dimensions (Figure 4*D*). When scanning with a much higher speed at the resonance peak around 700 Hz, the resulting bleached trajectory deviates significantly from the planned one (Figure 4E). However, the trajectory was stable; suggesting that resonance might be better controlled with optimized mechanical design and/or with the use of software corrections. To compensate for deviations from the planned trajectory in the 150 Hz regime, we used a manual approach. We repeatedly moved the

DOI:10.15774/PPKE.ITK.2015.003

points selecting the 3D trajectory in the *xy* plane while monitoring the basal fluorescence increase in the measured raw fluorescence traces until a better overlap between the 3D trajectory and the selected dendritic segment was visible.

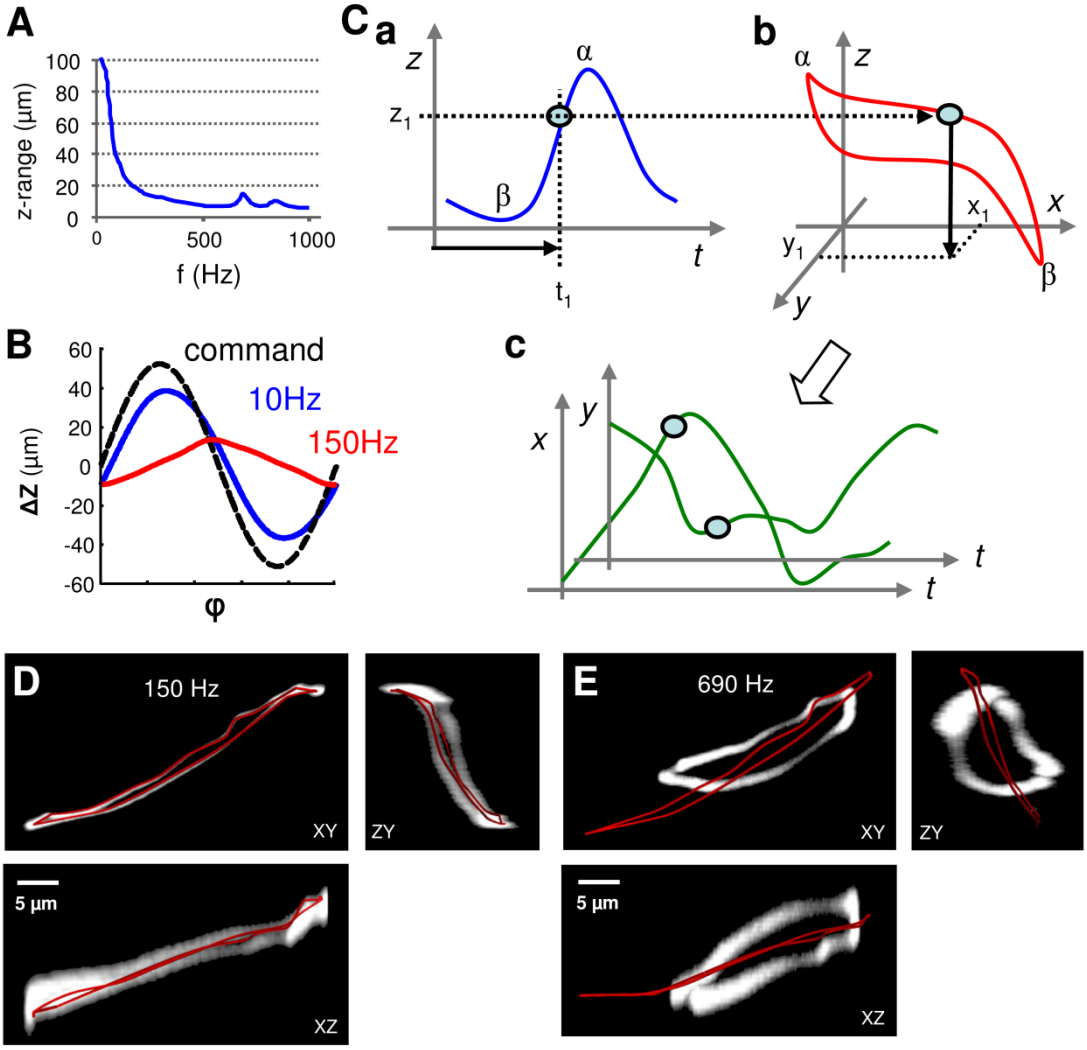

Figure 4 Roller Coaster Scanning.

*(**A**) The z-scanning range of the Roller Coaster Scanning as a function of repetition frequency. Note the resonance peak at 690 Hz. (**B**) Diagram showing the z-position of the objective as a function of time within a single oscillation period after the oscillation has become stable. The nonlinearity of the response is only apparent at higher frequencies. (**C**) Principle of calculating the Roller Coaster Scanning movement. (**Ca**) After 50-100 cycles (warm up period) the position of the objective reached a steady-state nonlinear response function (z(t)), the amplitude of which was set to be larger than the required z-scanning range in imaging. (**Cb**) For each t_1 time-point the location on the 3D trajectory was determined whose z coordinate equaled z(t_1). (**Cc**) The x and y coordinate projections of the 3D trajectory (x_1, y_1)*

DOI:10.15774/PPKE.ITK.2015.003

determined the x*(*t*) and* y*(*t*) functions which were used as command signal of the digital servo of the scanner motors. As illustrated in* **Cb***, the descending and ascending phase of the oscillation could cover different parts of the selected 3D trajectory. (***D***) Maximum intensity image stack projection of an originally homogeneous fluorescent sample after bleaching it along the user-selected 3D trajectory also used in Figure 5*A *and* B*. Measured intensities were inverted. User-selected 3D trajectory is overlaid in red. (***E***) The same measurement, but at the 690 Hz resonance peak. Note that although the measured trajectory did not follow the user selected one, it was stable suggesting that software correction is possible. On* D *and* E *scale bars apply for all panels. (Katona et al., 2011)*

We tested our method in biological measurements by scanning multiple spines of a CA1 hippocampal pyramidal cell simultaneously in 3D (Figure 5A) and by scanning long segments of dendrites of a CA1 interneuron (Figure 5B). Our approach resulted in a relatively limited, but biologically relevant *z*-scanning range (28 µm at 150 Hz, Figure 4*A*), while maintaining an advantageous FOV (650 x 650 μm^2 with 20x objective) and resolution parameters characteristic of two-photon microscopy near the theoretical diffraction limit. Namely, we tested two objectives: in the case of XLUPlanFI 20x (Olympus) FWHM of the PSF is 450 nm in XY and 2400 nm in Z and with the LUMPlanFI/IR 60x (Olympus) FWHM of the PSF is 430 nm in XY and 2300 nm in Z. Resonation frequencies 120-200 Hz were used for the biological measurements.

To estimate a measure of the benefit of Roller Coaster Scanning in our conditions, we first constructed the length statistics of dendritic sections gained after cutting reconstructed dendritic trees into slices parallel to the focal plane (Figure 5C Inset). Then for a given slice thickness representing available *z*-range, we calculated the percentage of the dendritic sections being larger than a threshold, thus being appropriate for a virtual measurement (Figure 5C). To derive a simple number expressing the benefit of our new method, we compared the access rate of the ideal axial resolution *z*-grab condition to the 7 - 25 µm *z*-grab conditions used in our experiments at the mean segment length of dendrites imaged in our study (42.3 ± 7.4 µm; range, 10–250 µm). The geometric mean of the ratios representing the two extremes is approximately 27. This means that using Roller Coaster Scanning we had approximately 27 times larger chance to image 40 µm dendritic segments than it would be with 2D scanning approaches.

DOI:10.15774/PPKE.ITK.2015.003

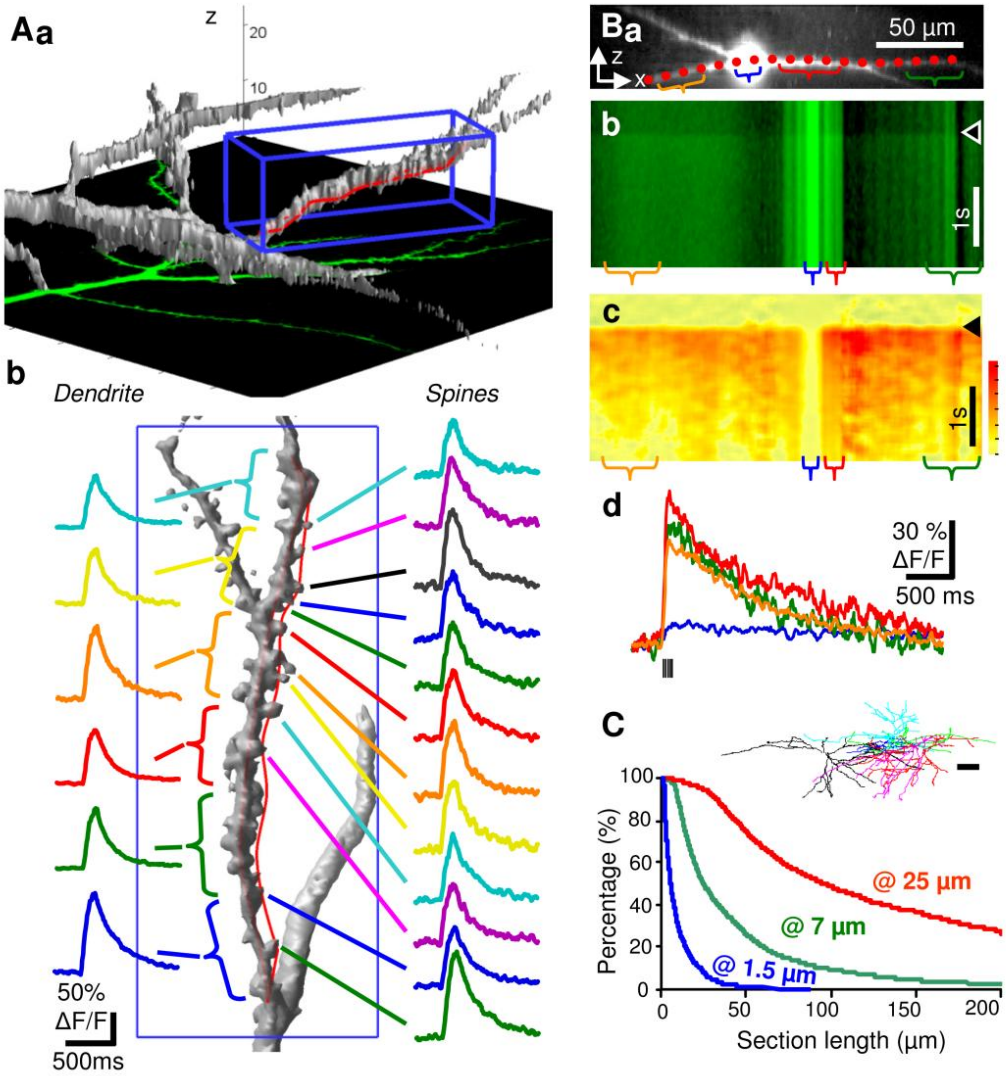

Figure 5 3D two-photon dendritic imaging at 150 Hz.

*(**Aa**) 3D reconstruction of a CA1 pyramidal cell dendritic segment. The red curve shows the 3D trajectory of the scanning crossing the dendritic segment and spines. The blue box is 15 x 15 x 37 µm^3. (**Ab**) Enlarged view of the blue box in **Aa**. A total of 18 regions including 12 spines located on the 3D scanning trajectory were measured simultaneously at 150 Hz. Ca^{2+} transients were induced by bAPs elicited by somatic current injection steps (5 APs, 35 Hz, average of 5 traces). (**Ba**) Maximum intensity side projection of a long CA1 interneuron dendrite. The pipette has been removed from the image. (**Bb**) 3D trajectory-scan measured along the dendrites in **Ba**. White open triangle indicates the time when bAPs were induced by somatic current injections (5 APs, 35 Hz, average of 5 traces). The horizontal axis is the spatial dimension along the measurement line (note that the scanning speed along the line is variable due to the nature of the Roller Coaster Scanning). Time is displayed along the vertical axis. (**Bc**) Relative fluorescence image (3D Ca^{2+} response) calculated from **Bb**.*

DOI:10.15774/PPKE.ITK.2015.003

*Colorbar: 0-63 % ΔF/F. (***Bd***) Individual Ca^{2+} transients measured in the color coded regions in* **Bb** *(black bars indicate current injections). Note the high SNR. (***C***) Access rate of long dendritic segments for 3D scanning shown at three different z-scan ranges. (Inset) Lateral projection of six reconstructed CA1 stratum radiatum interneurons used for this statistical calculation (scale bar: 100 µm). (Katona et al., 2011)*

3.2 NMDA spikes in stratum radiatum interneurons

To prove the method is beneficial in biological measurements, I describe here a study we performed on the dendrites of inhibitory interneurons. Inhibitory interneurons are considered to be the controlling units of neural networks, despite their sparse number and unique morphological characteristics when compared to excitatory pyramidal cells. Though pyramidal cell dendrites have been shown to display local regenerative events – dendritic spikes – evoked by artificially patterned stimulation of synaptic inputs (Schiller et al., 2000; Magee and Johnston, 2005), no such studies existed for interneurons or for spontaneous events. In addition, an imaging technique needed to be developed that have the required spatial and temporal resolution for the detection of spontaneously occurring events that trigger dendritic spikes. Using Roller Coaster Scanning, we found that localized dendritic spikes can be observed in hippocampal CA1 stratum radiatum interneurons during spontaneous network activities *in vitro* (Figure 6). In these experiments where we searched for spontaneous dendritic spikes, slices were placed into a dual-superfusion slice chamber (the tissue slice lies on a mesh allowing flow of the perfusion fluid also under the tissue) to maintain physiologically relevant network activity (Hajos et al., 2009).

Spontaneous dendritic spikes were reproduced using synaptic stimulation and two-photon glutamate uncaging (see 3.4 Materials and methods) to be able to investigate their pharmacological properties and their dependence on the number and distribution of coincident synaptic inputs driving them. These proved dendritic spikes to be NMDA channel driven by their sensitivity to the selective blocker AP5 (D-2-Amino-5-phosphonovaleric acid), but voltage gated Na^+ and Ca^{2+} channels did not play significant role. Simulating synaptic inputs with two-photon glutamate uncaging showed that these NMDA spikes appear when ~10 spatially clustered inputs arrive synchronously and trigger supralinear integration in relatively small (~14 µm) dynamic interaction zones (Katona et al., 2011).

DOI:10.15774/PPKE.ITK.2015.003

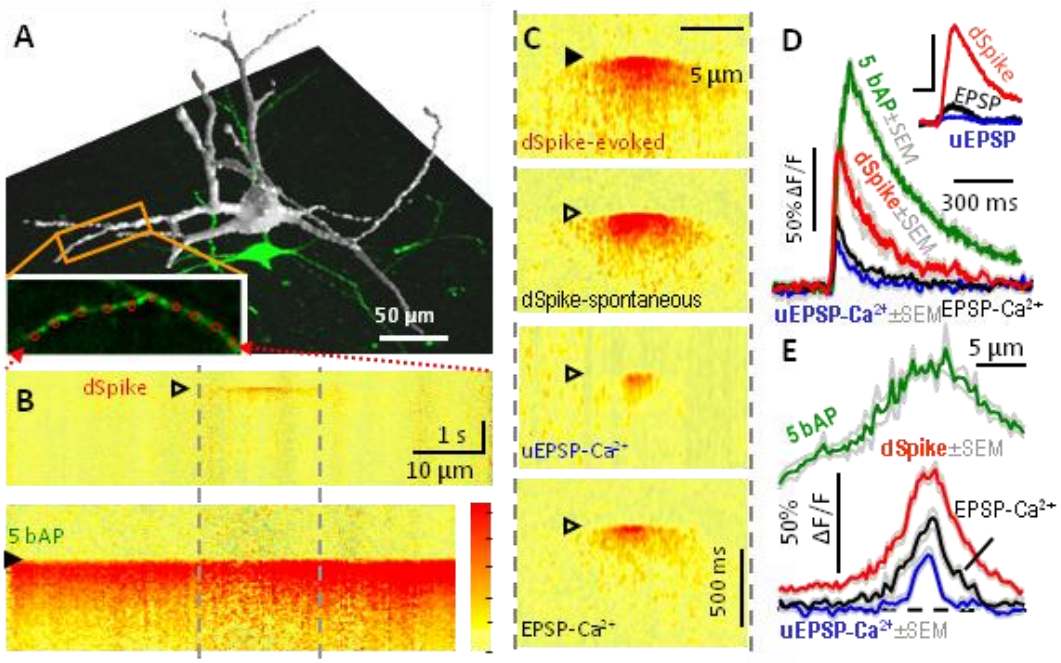

Figure 6 Spontaneous and CA3 stimulation-induced subthreshold dendritic spikes. *(**A**) 3D reconstruction of an interneuron. Long dendritic segments (*inset*) were systematically imaged to find spontaneous or CA3 stimulation-induced synaptic responses. (**B**) Spatially normalized 3D dendritic Ca^{2+} transients (3D Ca^{2+} responses; colorbar: 0-63% ΔF/F; dendritic length was 76 µm) showing a well compartmentalized spontaneous synaptic response (*top*) and a more homogeneous response evoked by 5 bAPs (*bottom*). (**C**) 3D Ca^{2+} responses representing types of spontaneous events (*empty triangles*) and response following CA3 stimulation (*filled triangle*) in a dendritic region from panel* B *(marked with* gray dashed *lines). (**D**) Ca^{2+} transients (average of 5-7 traces) derived at the peak of the 3D Ca^{2+} responses in* B *and* C. Inset*, Corresponding somatic membrane voltage (scale bars: 4 mV and 15 ms). (**E**) Spatial distribution of peak 3D Ca^{2+} responses in* B *and* D. Gray traces *show mean ± SEM (Katona et al., 2011)*

3.3 Discussion

Our observations of local dendritic spikes in thin dendrites of interneurons were facilitated by more factors. We have used a new recording chamber with dual superfusion to maintain physiologically relevant network activities through better oxygen supply (see 3.4 Materials and methods). We developed Roller Coaster Scanning, increasing access rate to imaging long continuous dendritic segments. This second feature, with the preserved high spatial and temporal resolution, allowed us to precisely localize the sites and properties of spontaneous

DOI:10.15774/PPKE.ITK.2015.003

(and evoked) individual inputs, as well as their spatially and temporally patterned combinations during integration of multiple synaptic inputs arriving onto a dendritic segment.

The optical pathway of the Roller Coaster microscope is simple, and does not contain any material beyond the objective that introduces angular or linear dispersion or laser intensity loss, therefore

- the good spatial resolution characteristic of two-photon microscopy are preserved,
- experiments requiring high energy pulses like two-photon uncaging, bleaching, ablation or *in vivo* imaging of deep tissue (Helmchen and Denk, 2005) are achievable
- the combination of Roller Coaster Scanning with new optical methods such as for example the already mentioned high resolution imaging technique STED is theoretically possible.

These properties make Roller Coaster Scanning ideal for scanning extensive and continuous dendritic segments with high spatial and temporal resolution.

3.4 Materials and methods

Slice preparation and electrophysiology. Acute hippocampal slices were prepared from 16-20 day old Wistar rats using isoflurane anesthesia followed by swift decapitation, in accordance with the Hungarian Act of Animal Care and Experimentation (1998; XXVIII, section 243/1998.). Coronal (300 μm) or horizontal (450-600 μm) brain slices were cut with a vibratome and stored at room temperature in artificial cerebrospinal fluid (ACSF) (in mM: 126 NaCl, 2.5 KCl, 2 $CaCl_2$, 2 $MgCl_2$, 1.25 NaH_2PO_4, 26 $NaHCO_3$ and 10 glucose) as previously described (Rozsa et al., 2004). The 450-600 μm thick horizontal slices were used in the experiments involving spontaneous dSpikes and were recorded in a custom-made recording chamber where improved oxygenation could be achieved by simultaneous perfusion of both the top and the bottom surfaces of the slices (Hajos et al., 2009). Preventing bubbles from entering into the recording chamber allowed long term optical measurements.

Hippocampal neurons in CA1 stratum radiatum near the border of the stratum lacunosum-moleculare were visualized using 900 nm infrared lateral illumination. Current-clamp recordings were made at 32 °C (MultiClamp 700B, Digidata 1440; Molecular Devices,

DOI:10.15774/PPKE.ITK.2015.003

Sunnyvale, CA, USA) with glass electrodes (6–9 MΩ) filled with (in mM): 125 K-gluconate, 20 KCl, 10 HEPES, 10 Di-Tris-salt phosphocreatine, 0.3 Na-GTP, 4 Mg-ATP, 10 NaCl, 0.06 Oregon Green BAPTA-1 (OGB-1, Invitrogen) and biocytin. Cells with a resting membrane potential more negative than –50 mV were accepted.

Focal synaptic stimulation was performed by 6-9 MΩ glass electrodes filled with ACSF were placed at a distance of 10-25 µm from the dendrite (stimulation: 0.1 ms, 10-50 V, 10 ms pulse interval at double pulses; Supertech Ltd., Pécs, Hungary). Backpropagating APs were induced by somatic current injections (200–400 pA, 5 ms; 5 bAPs were evoked at 35 Hz). The NMDA receptor selective antagonist AP-5 (60 µM) was injected by a motion artifact-free rapid perfusion system as described earlier (Rozsa et al., 2008), whereas bicuculline (20 µM) was applied in the bath. All evoked EPSPs were verified for synaptic delay.

Stimulation of Schaffer collaterals at the hippocampal CA3 area (1-5 stimuli, 100 Hz, 35-65 V) was applied via the same method as used for focal synaptic stimulation, with the exception that the stimulatory pipette of 4-5 MΩ was placed in the pyramidal layer of CA3.

All chemicals and drugs unless otherwise noted were purchased from Sigma (St Louis, MO, USA). Data acquisition was performed using either pClamp8 or pClamp10 (Molecular Devices) and MES (Femtonics Ltd.) software.

Three dimensional two-photon imaging. Real-time, 3D two-photon imaging was performed using a modified two-photon microscope (Femto2D, Femtonics) enabling scanning along 3D trajectories that cross neuronal processes in 3D (Roller Coaster Scanning) using a customized piezo actuator (P726, PhysikInstrumente) for z-scanning. Resonation frequencies 120-200 Hz were used in other physiological measurements. Femtosecond lasers (Mai Tai HP, SpectraPhysics, Mountain View, CA) were tuned to 800-840 nm for imaging.

Two-photon uncaging. Photolysis of caged glutamate MNI-glutamate (2.5 mM; Tocris) or MNI-glutamate trifluoroacetate (2.5 mM; Femtonics) was performed with 720 nm ultrafast, dispersion compensated pulsed laser light (Mai Tai HP Deep See) controlled with an electro-optical modulator (Model 350-80 LA). Three dimensional imaging (at 840 nm) was limited to < 7 µm z-scanning ranges in uncaging experiments. Scanning was interleaved with two-photon glutamate uncaging periods when galvanometers jumped to the maximum 38

DOI:10.15774/PPKE.ITK.2015.003

selected locations (< 60 μs jump time) and returned back to the measurement trajectory thereafter.

Calcium imaging. Two-photon imaging started 15-20 min after attaining the whole-cell configuration. The spatially normalized and projected Ca^{2+} response (defined as 3D Ca^{2+} response) was calculated from the raw 3D line-scan, F(d,t) by applying the $\Delta F/F=(F(d,t)-F_0(d))/F_0(d)$ formula where d and t denote distance along the curve and time respectively, and $F_0(d)$ denotes the average background-corrected prestimulus fluorescence as a function of distance along the curve. All 3D Ca^{2+} responses are color coded (colors from yellow to red show increasing Ca^{2+} responses, 0–63 % ΔF/F), and projected as a function of d and t.

At the end of each experiment, a series of images across the depth of the volume encompassing the imaged neuron was taken. Measurement control, real-time data acquisition and analysis were performed with a MATLAB based program (MES, Femtonics Ltd., Budapest) and by software written in our laoratory.

Statistics. Unless otherwise indicated, data are presented as means±SEM Statistical comparisons were performed using the Student's paired t-test.

3.5 Thesis

Thesis 2*: I developed a new method to measure activity across neurons by using a new implementation of piezoelectric objective positioning and a new driving principle. The method is capable of depth-scanning ten times faster than previous realizations. I experimentally proved the usability and parameters of the method.*

Publication related to the thesis: Katona et al., 2011.

Using scanning mirrors to deflect the laser beam enables rapid positioning of the focal point only in the focal plane of the objective. Biological structures are, however, rarely planar. Our aim was to sample activity along long tortuous dendritic segments so we needed to develop a method capable of scanning 3D trajectories with high speed.

We extended our two-dimensional Multiple Line Scanning Method with the use of a high-speed, piezoelectric objective positioner to image points along a 3D trajectory with high spatial as well as temporal resolution. Line-scanning using galvanometric mirrors was precisely synchronized to the phase of the *z*-axis movement of the nonlinearly resonating

DOI:10.15774/PPKE.ITK.2015.003

objective. We named this method Roller Coaster Scanning (Katona et al., 2011). The method allows *in vitro* imaging of up to 250 µm long dendrites situated in a wide field of view (up to 650 µm x 650 µm). It has a suitable *z*-scanning range (up to 25 µm) with a resolution characteristic of two-photon microscopy (< 450 nm) and enables high repetition rates (150-690 Hz) without limiting pixel dwell time. Using Roller Coaster Scanning we had approximately 27 times larger chance to image 40 µm dendritic segments than we would have had with 2D scanning approaches.

These parameters allowed us to detect spontaneous events on spatially extensive dendritic arbors of hippocampal CA1 stratum radiatum interneurons (Katona et al., 2011). Here we searched for active synaptic inputs on long dendritic segments of these interneurons during spontaneous network activities *in vitro* and found spatially extensive dendritic spikes and small compartmentalized unitary events. These events were reproduced using focal electrical stimulation and two-photon glutamate uncaging to be able to investigate their pharmacological properties and their dependence on the number and distribution of coincident synaptic inputs driving them. We found that NMDA dependent dendritic spikes appear when ~10 spatially clustered inputs arrive synchronously and trigger supralinear integration in relatively small (~14 µm) dynamic interaction zones.

DOI:10.15774/PPKE.ITK.2015.003

4 ACOUSTO-OPTIC DEFLECTOR BASED 3D SCANNING (THESIS 3)

In the third step of developments our goal was to create a two-photon microscope capable of scanning 3D ROIs in random order thereby overcoming mechanical limits posed by earlier solutions. An ideal 3D microscope for neuroscience applications needs to simultaneously satisfy two different needs in the largest possible scanning volume. The first need is to record activity across the dendritic tree of a single neuron at high spatial and temporal resolution in 3D in a way that dendritic spines remain resolvable. The second is to record in an extensive volume at high speed in order to capture activities of a large number of cell bodies in a neuronal population.

4.1 Why acousto-optical scanning?

Several technologies have been developed to generate 3D readouts of fast population and dendritic activities, including liquid lenses (Grewe et al., 2011), deformable mirrors, temporal and spatial multiplexing (Durst et al., 2006; Cheng et al., 2011), axicon or planar illumination-based imaging (Holekamp et al., 2008), fast *z*-scanning based on an axially moving mirror (Botcherby et al., 2012), holographic scanning (Nikolenko et al., 2008), piezo-scanning with sinusoidal and non-linear resonance (Gobel et al., 2007; Katona et al., 2011), simultaneous multiview light-sheet microscopy (Tomer et al., 2012), and optical fiber acousto-optical (AO) deflector based 3D scanning (Rozsa et al., 2007). AO scanning technology has also been used to rapidly change beam focusing without mechanical movement (Kaplan et al., 2001), and AO technology for two-photon microscopy has been adapted in several applications (Kaplan et al., 2001; Reddy and Saggau, 2005; Iyer et al., 2006; Salome et al., 2006; Rozsa et al., 2007; Vucinic and Sejnowski, 2007; Duemani Reddy et al., 2008; Otsu et al., 2008; Grewe and Helmchen, 2009; Grewe et al., 2010; Kirkby et al., 2010).

However, in 2012 there were limitations in the use of these methods for 3D optical recordings both *in vitro* and *in vivo*. In *in vitro* applications, new 3D technologies either were

DOI:10.15774/PPKE.ITK.2015.003

not validated in functional measurements on biological samples (Kaplan et al., 2001; Reddy and Saggau, 2005; Durst et al., 2006; Rozsa et al., 2007; Kirkby et al., 2010) or they did not simultaneously fulfill a set of technical criteria which are necessary to follow propagation of APs or Ca^{2+} spikes in dendrites over hundreds of micrometers.

Namely,

- less than 30 µm z-scanning were shown (Kaplan et al., 2001; Reddy and Saggau, 2005; Iyer et al., 2006; Salome et al., 2006; Rozsa et al., 2007; Vucinic and Sejnowski, 2007; Duemani Reddy et al., 2008; Holekamp et al., 2008; Nikolenko et al., 2008; Otsu et al., 2008; Grewe and Helmchen, 2009; Grewe et al., 2010; Kirkby et al., 2010; Katona et al., 2011),
- less than 20 measurement points were shown (Kaplan et al., 2001; Stosiek et al., 2003; Reddy and Saggau, 2005; Durst et al., 2006; Salome et al., 2006; Rozsa et al., 2007; Vucinic and Sejnowski, 2007; Duemani Reddy et al., 2008; Nikolenko et al., 2008; Grewe and Helmchen, 2009; Kirkby et al., 2010; Grewe et al., 2011; Botcherby et al., 2012),
- or less than 100 Hz repetition rate were demonstrated (Durst et al., 2006; Salome et al., 2006; Gobel et al., 2007; Rozsa et al., 2007; Nikolenko et al., 2008; Cheng et al., 2011; Grewe et al., 2011; Tomer et al., 2012) in these previous studies.

Regarding *in vivo* applications, random-access recording of the activity of hundreds of selected neurons situating in 3D was not validated until 2012. After we had published our 3D microscope (Katona et al., 2012) two other groups also published biological results with the use of 3D AO microscopes, however their 3D scanning volume is still an order of magnitude smaller than our scanning volume and they have shown less number of cells recorded simultaneously and smaller depth penetration (Cotton et al., 2013; Fernandez-Alfonso et al., 2014).

As mentioned in chapter 2.2, AO scanning as single-point two-photon ROI scanning approach can significantly increase the SNR of the signal measured from a ROI in a unit time, as compared to classical raster scanning. Quantitatively, by modifying Equation 3 to the 3D case yields:

DOI:10.15774/PPKE.ITK.2015.003

Equation 4. $$(SNR\ gain) = \sqrt{\frac{total\ image\ volume}{volume\ covered\ by\ the\ ROIs}}$$

In a typical *in vivo* measurement, when we consider using a 450 x 450 x 650 μm^3 scanning volume (Katona et al., 2012) and measure 100 neurons of diameter of 10 µm, random access scanning will provide a 50 fold gain in the SNR.

4.2 Principles

The phrase “acousto-optic” refers to the field of optics that studies the interaction between sound and light waves. The sound generated pressure fluctuations cause a periodic change in the refractive index of the medium (usually tellurium dioxide) which behaves like an optical grating: diffracting light according to its period length and the wavelength of the light.

4.2.1 Acousto-optical deflection

AO deflectors control the direction of the optical beams by ultrasonic waves. During operation, ultrasonic waves induced via a piezoelectric transducer diffract the laser beam depending on the driving frequency of the transducer (Kaplan et al., 2001). The change of the diffraction angle is given by

Equation 5. $$\Delta\Theta_d = \frac{\lambda}{\nu}\Delta f$$

where λ is the optical wavelength of the beam, ν is the velocity of the acoustic wave, and Δf is the change of the sound frequency (Figure 7). Diffracted beam amplitude depends on a number of geometrical parameters and the acoustic energy (Veress et al., 2010). The device is ideal for random-access beam positioning as the frequency of the driving voltage can be changed quickly, thus beam steering is not limited by mechanical inertia of any moving parts.

DOI:10.15774/PPKE.ITK.2015.003

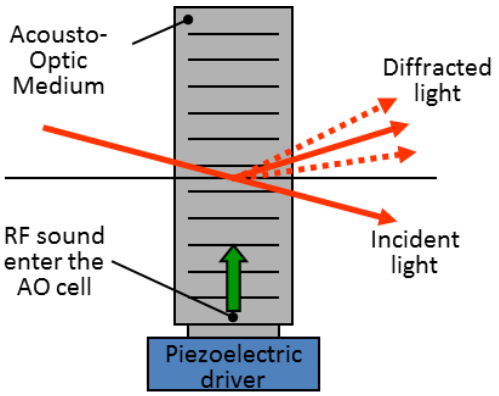

Figure 7 Operating principle of AO deflectors.

A piezoelectric driver elicits radio frequency (RF) sound waves due to the externally applied sinusoidal voltage. Sound enters and traverses through the diffracting (TeO_2) medium while interacting with light throughout the aperture. Light is diffracted on the refraction index changes of the sound wave as on a steady optical grating, providing diffracted light beams whose angle is dependent on the frequency of the driving.

4.2.2 Acousto-optical focusing

Besides deflection, AO deflectors can also be used for fast focal plane shifting (Kaplan et al., 2001; Katona et al., 2012; Cotton et al., 2013; Fernandez-Alfonso et al., 2014). If the optical aperture is filled with acoustic waves the frequency of which increases as a function of time (chirped wave), different portions of the optical beam are deflected in different directions (Figure 8). As a result, a focusing or defocusing effect occurs, depending on the frequency slope (sweep rate) of the chirped acoustic wave. The focal length (F) of an AO lens can be calculated from the sweep rate as

Equation 6. $$F = \frac{v^2 T_{scan}}{2\lambda \Delta f}$$

where λ is the optical wavelength of the beam, v is the velocity of the acoustic wave, Δf is the change of the sound frequency and T_{scan} is the modulation rate of the sound frequency (Kaplan et al., 2001).

DOI:10.15774/PPKE.ITK.2015.003

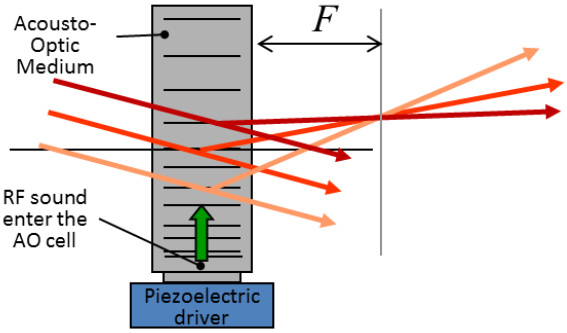

Figure 8 Acousto-optical focusing.

AO deflector arrangement similar to Figure 7, but here the sound frequency is changing (chirped wave), resulting in a varying grating constant along the propagation axis. As a consequence, different parts of the laser beam are diffracted with varying angles creating a focus point whose position can be changed by the parameters of the sound applied to the deflector. Red and orange lines indicate laser beams, F denotes focal distance.

To keep the focus stable, the gradient of the frequency should be constant in the crystal. The frequency should therefore be linearly increased (or decreased) at the piezoelectric driver to preserve the focal distance. This will result in a lateral drift of the focal point which can be compensated by a second AO deflector with a counter-propagating sound wave (Kaplan et al., 2001).

The optical grid generated within the AO deflector is equivalent to a cylindrical lens, focusing along only one dimension. In 3D two-photon microscopy we need to scan points in all three dimensions, therefore, a combination of two, perpendicularly oriented cylindrical lenses with the same focal distance are required. As both AO lenses (*x*, *y*) require drift compensation, 3D microscopes need (at least) four AO deflectors (x1, y1, x2, y2). The four AO deflectors can be optically coupled using afocal projections (telescopes with two lenses where the distance between the lenses is equal to the sum of each lenses' focal length) and air in different combinations.

DOI:10.15774/PPKE.ITK.2015.003

4.3 Realizing the acousto-optic 3D microscope

4.3.1 Optical design

A detailed optical model was set up to find those combinations of all active and passive optical elements in the scanning light-path of the microscope which would provide the maximal exploitation of the apertures of all lenses within the 20× objective (numerical aperture, NA = 0.95) at different *x*, *y*, and *z* scanning positions, and therefore result in the smallest PSF in the largest possible scanning range (See 4.8 Materials and methods).

The model suggested a new design concept. The largest scanning volume can be reached by grouping the deflectors into two functionally distinct groups which are coupled by one afocal projection (Figure 9).

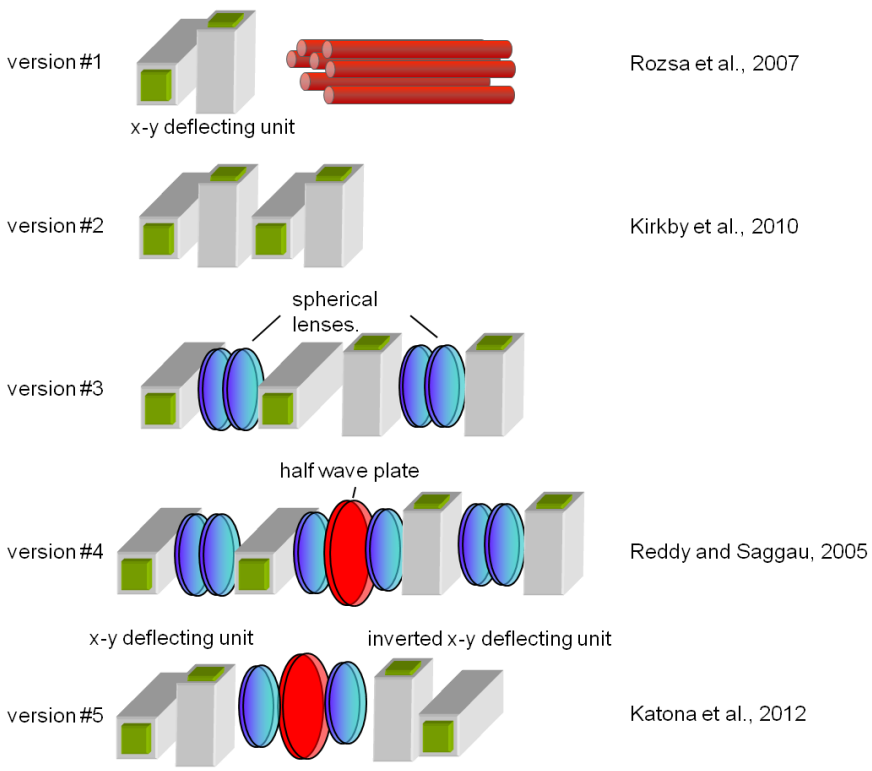

Figure 9 Different 3D AO scanning arrangements.

Version #1 uses optical fibers to position the excitation beam in 3D (Rozsa et al., 2007), however it has been difficult to implement this version due to the requirement of many mechanical devices positioning the fibers. Versions #2-5 were analyzed by modeling and Version #5 was found the most beneficial to implement (Katona et al., 2012). Version #2 (Kirkby et al., 2010; Fernandez-Alfonso et al., 2014) and Version #4 (Reddy and Saggau,

DOI:10.15774/PPKE.ITK.2015.003

2005; Iyer et al., 2006; Duemani Reddy et al., 2008; Cotton et al., 2013) have been described by other laboratories and have recently been used for functional measurements (Cotton et al., 2013; Fernandez-Alfonso et al., 2014) but – according to our expectation from optical modeling – they have lower specifications than our solution.

4.3.2 Construction of the 3D AO microscope

According to the arrangement suggested by our optical model (version #5 on Figure 9) (Katona et al., 2012), a large-aperture (15-17 mm) optical assembly was constructed (Figure 10). A Ti:sapphire laser provides the excitation pulses. Due to the slightly different refraction index of materials at different wavelengths, ultrashort pulses broaden when travelling through any material as the phase of the different Fourier components of the wave shift relative to each other. To cancel out this effect leading to a drop of two-photon excitation at the sample level, the laser source incorporates an automated compensating unit to eliminate temporal pulse broadening caused by the forthcoming optical assembly (prechirping). On top of the adjustable prechirping provided by the laser source, a fixed four-prism sequence (Proctor and Wise, 1992) adds a large negative second- and third-order dispersion (−72,000 fs^2 and −40,000 fs^3) in order to cancel out the majority of the dispersion (dispersion compensation unit, Figure 10). We used the laser source to fine-tune compensation by optimizing fluorescence at the sample. A Faraday isolator blocks the coherent back reflections. An automated beam stabilization unit is necessary to precisely stabilize the laser beam in the long optical pathway, and cancel out subtle thermal drift errors. The beam stabilization unit is built from position sensors (quadrant detectors) and motorized mirrors, wired in a feedback loop. The beam is then magnified by a beam expander to match the large apertures (15 mm) of the first pair of AO deflectors. These deflectors form two orthogonal electric cylinder lenses filled with continuously changing frequency (“chirped”) acoustic waves (Kaplan et al., 2001), and are used for *z*-focusing (AO *z*-focusing unit). Next, laser beams from the *x* and *y* cylindrical lenses are projected to the *x* and *y* AO deflectors (17 mm apertures) of the 2D-AO scanning unit, respectively, by telecentric projection. The 2D-AO scanning unit performs lateral scanning and also compensates for the lateral drift of the focal point generated by the cylindrical lenses during *z*-focusing (Kaplan et al., 2001) (drift compensation). The angular dispersion compensation unit (a lens pair designed to cancel out angular dispersion caused by the AO deflectors)

DOI:10.15774/PPKE.ITK.2015.003

optically links the 2D-AO scanning unit and the objective. Finally, the 3D scanning system is coupled to a 2D two-photon microscope in which fluorescent signals are collected by PMTs fixed directly onto the objective arm for high photon-collection efficiency. See details in 4.8 Materials and methods.

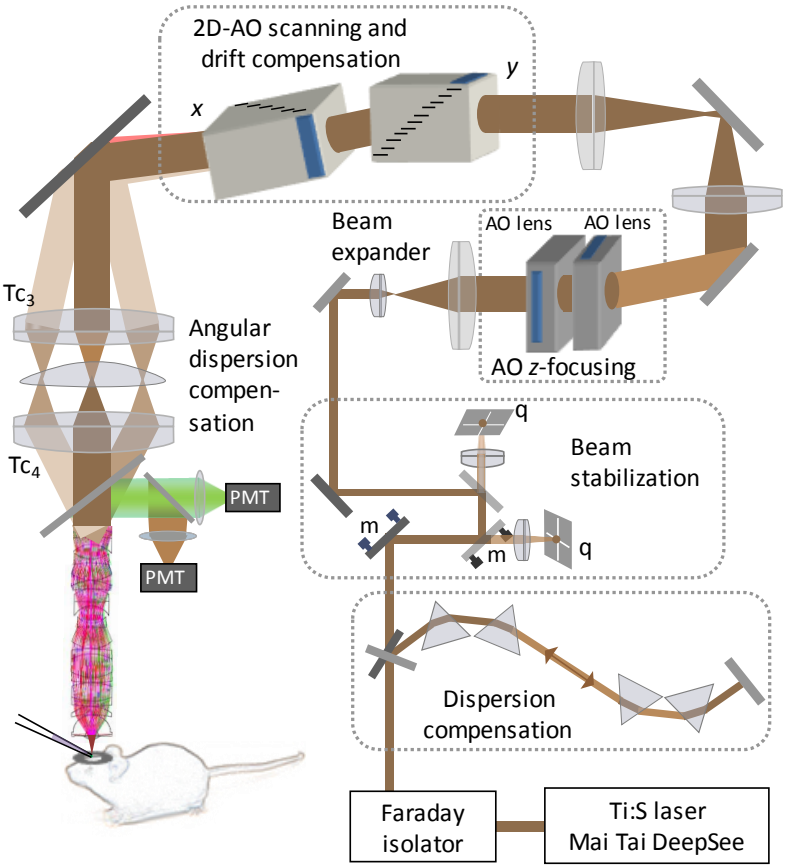

Figure 10 Schematics of the 3D AO microscope setup.

The AO deflectors were grouped in two functional groups coupled with an afocal projection. The output of the second, 2D-AO scanning crystal group was coupled into a two-photon microscope equipped with non descanned PMTs. Complex dispersion compensating and beam stabilizing optics was necessary between the laser and the AO scanner. (Katona et al., 2012)

4.3.3 Controlling 3D AO scanning

To focus the excitation beam to a given *x*,*y*,*z*-coordinate, the four AO deflectors should be driven with synchronously varying frequency voltage signals. The position and the movement of the focal point is determined by eight values, four of them control the starting acoustic frequency on the four AO deflector drivers, while the other four defines the

DOI:10.15774/PPKE.ITK.2015.003

frequency ramp speeds (chirping). We used four direct digital synthesizer chips (AD9910, Analog Devices) to generate sinusoidal waves with linearly changing frequencies for the four AO deflectors. The chips were built on custom designed multilayer printed circuit boards (AO driver cards) incorporating FPGA (field-programmable gate array, Xilinx) chips to connect them into the Femto2D microscope's communication system (Figure 11) and to route the necessary synchronization signals.

Figure 11 Custom designed electronic cards for the electronic system

Left, picture of the universal analog I/O and PMT digitizer card. Right, picture of the AO driver card.

AD9910 is a complex signal generation device featuring 22 64 bit registers and various clocking, I/O and signal generation modes. The serial input-output port of the chip was used to access the registers for programming and data upload. Frequencies were generated using the 'Digital Ramp Generation' (DRG) mode of the chip, allowing internal generation of linearly changing frequencies. The diffraction efficiency of each AO cell at a given acoustic power has particular frequency dependence, therefore, signal amplitudes were generated parallel to the frequency generation using the 'RAM Playback Operation' mode of the chip allowing arbitrary amplitude form generation. We uploaded a frequency-amplitude profile to each chip's internal RAM (random access memory), so when it was played back, the actual amplitude read from the RAM matches the actual frequency played from the DRG mode. This way, we could compensate for signal loss at the side of the field of view and also for the amplitude inhomogeneity resulting from the fact that AO deflector driving frequencies continuously change during one focusing event (dynamic power compensation).

We used the following fairly simple empirical method to calculate from the desired location the frequency and chirp parameters for the AO deflectors. The final equations are formed

DOI:10.15774/PPKE.ITK.2015.003

according the optical theory (Kaplan et al., 2001), but constants are determined experimentally, furthermore modifying factors are added to introduce there degrees of freedom for optical error compensation. The parameters of the frequency generation are calculated as follows:

Equation 7.

$$
\begin{aligned}
freq_{x1} &= center_{X1} \\
freq_{x2} &= center_{X2} - X \\
freq_{y1} &= center_{Y1} \\
freq_{y2} &= center_{Y2} - Y \\
\\
chirp_{x1} &= (Z+e) \\
chirp_{x2} &= (1+d).*(Z+e) \\
chirp_{y1} &= (Z-e)./(1+c/32*Z) \\
chirp_{y2} &= (1+d).*(Z-e)./(1+c/32*Z)
\end{aligned}
$$

Where `freq` and `chirp` parameters are the requested output variables. `X`, `Y` and `Z` are the coordinates of the desired focal point relative of the center of the FOV scaled with a constant value depending on the objective's magnification. `c`, `d`, `e` parameters are used to dynamically compensate for various optical errors (dynamic error compensation). The four crystals are termed according to their function x1, y1, x2 and y2. `center` is the middle of the crystals' bandwidth. The optimal compensation parameters were determined in advance for each point of the scanning volume. During this optimization process we varied the c,d,e parameters at different positions in the FOV in order to maximize the fluorescence intensity and the sharpness of fluorescent beads.

The 55 MHz bandwidth of the AO deflectors used in the 2D AO scanner unit can be addressed with 4 kHz accuracy, providing a resolution of 13,750 pixels, equivalent to 51 nm spatial accuracy (discretisation) for the ~700 µm FOV. The relatively reduced bandwidth of deflectors used in the AO *z*-focusing unit (40 MHz) corresponds to 10,000 independent positions and, therefore, 140 nm focusing accuracy. As both lateral and axial accuracy is much smaller than the PSF (470 nm, 490 nm, 2,490 nm along the *x*, *y*, *z* axes, respectively) we have sufficient precision of positioning the focal point practically anywhere in the FOV.

Because AO deflectors have limited electrical bandwidth, the frequency change can be maintained only for a limited time, and then the frequency has to be reset. This sudden change in frequency results in a distorted focal point for a short period of time and can therefore be considered as 'dead time' (Figure 12). The length of this period is defined by

DOI:10.15774/PPKE.ITK.2015.003

the time taken by the acoustic wave to travel through the aperture of the crystal. This depends on the size and material of the AO deflectors as well as the acoustic mode and usually takes around 10 microseconds.

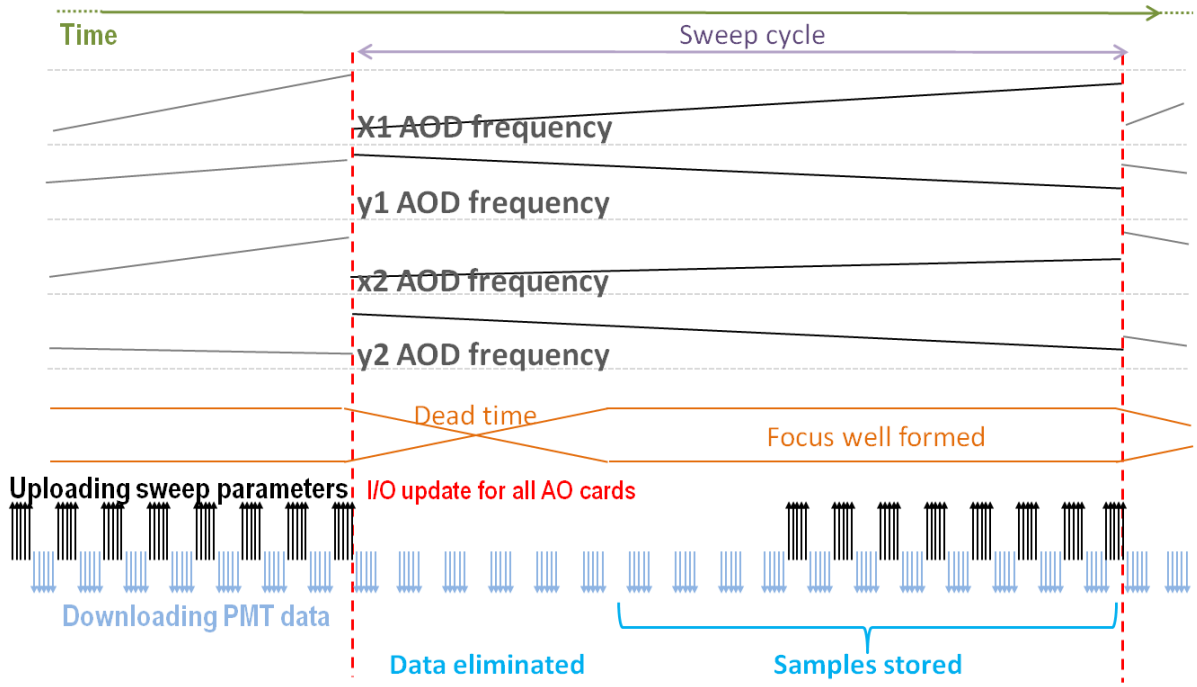

Figure 12 Driving functions and timing of operation of the four-deflector sequence. *(Top) The four upper traces show the frequency modulation of the sine wave as a function of time for the four AO deflectors (x1, y1, x2, y2) within* one and a half sweep cycles*. This results in dead times and periods when focus is well formed (orange). (Bottom) PMT data are continuously collected and transferred to the computer, however PMT data collected during the dead time period is eliminated during the acquisition. Red dashed lines show the synchronous frequency reset of all driver functions. (Katona et al., 2012)*

All the eight parameters determining the position and the movement of the focal point are updated in every sweep cycle (usually 33.6 µs is used, the reasonably minimum – because of the dead time is around 10 µs). During each sweep cycle all PMT channels are sampled multiple times (Figure 12). In the simplest case, the goal is to attain a steady focal spot without lateral drifting (random-access scanning mode). In this scanning mode, retained PMT data are averaged (separately for each channel) and one value is created for each measurement cycle, corresponding to a single point in 3D. Therefore in this averaged mode on which 3D random-access scanning is based, the repetition speed of a ROI depends only

DOI:10.15774/PPKE.ITK.2015.003

on the number of points (practically we used points between 2 and 2,000 for the measurements). It is also possible to let the focal spot drift in a controlled manner and take the measurement data separately (without averaging), enabling more complex measurement modes in the future.

We extended the microscope control software used in the previous chapters, and added new measurement modes for *xy* scanning, 3D Multiple Line Scanning and *z*-stack creation using the AO scanner. We also added new cell localization, point handling and trajectory selecting tools supporting the 3D requirements. We added a 3D virtual reality environment to the system (Figure 13, 4.8 Materials and methods). Using 3D visualization and user interface not only significantly enhanced manual ROI selection but also allowed verification and correction of the automatically selected measurement locations. Finally, we also added new data analysis routines supporting 3D random access point measurement data.

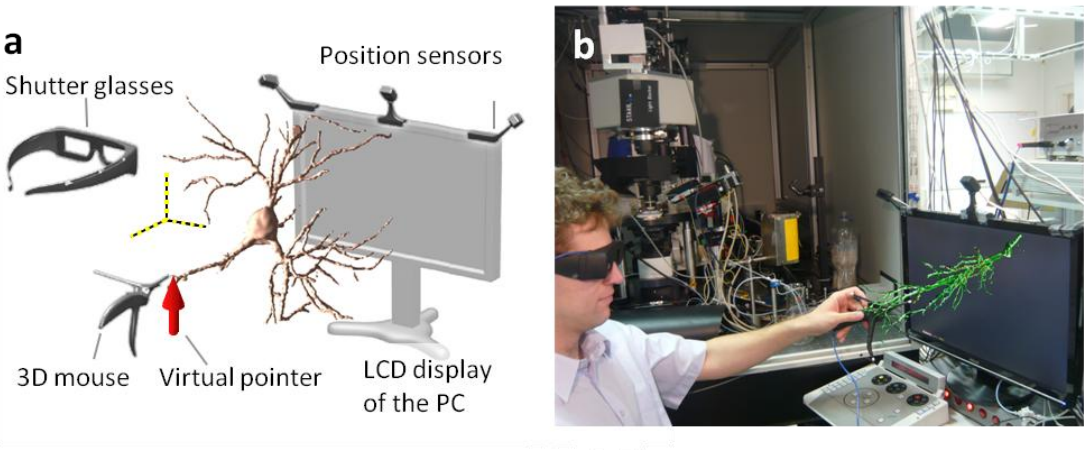

Figure 13 3D virtual reality environment for 3D two-photon imaging.

*(**a**) With the help of the 3D virtual reality environment, the 3D measurement locations can be freely modified or observed from any angle. Head-tracked shutter glasses ensure that the virtual objects maintain a stable, "fixed" virtual position even when viewed from different viewpoints and angles, i.e. the cell's virtual coordinate system is locked in space when the viewer's head position changes; however, it can be rotated or shifted by the 3D "bird" mouse. The bird also allows the 3D measurement points to be picked and repositioned in the virtual 3D space of the cell. See also 4.8 Materials and methods. (**b**) Image of the 3D AO setup and the experimenter using the 3D virtual reality environment. (Katona et al., 2012)*

DOI:10.15774/PPKE.ITK.2015.003

4.4 Characterizing the performance of the 3D AO microscope

To test the performance of our microscope, first we imaged fluorescent beads located in 3D to see if the microscope can focus and stabilize the focal point at different depths. We used the 20× objective (Olympus XLUMPlanFI20x/0.95) whose parameters were also used in optical modeling. Fluorescence signals were measured by repetitively AO-scanning the selected points only, using a 16.8 µs pixel dwell time and a 10-20 µs (typically 16.8 µs) positioning time with repetition rates from 23.8/N kHz to 54.3/N kHz (N denotes the number of points ranging from 2 to 2,000; Figure 14).

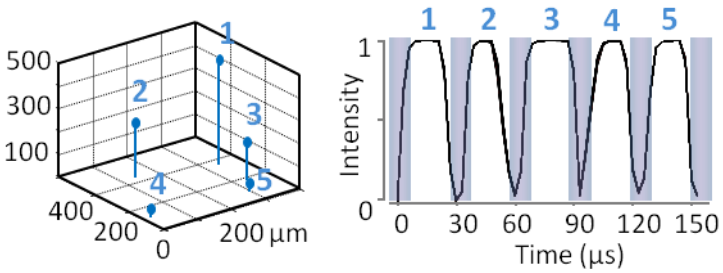

Figure 14 Stability of 3D AO scanning in random-access mode.

(Left) Location of five fluorescent beads (6 µm) was repetitively scanned in a 3D sample. (Right) Five overlaid fluorescence measurements showing dead times and windows of properly formed and positioned focal point. (Katona et al., 2012)

Then we determined the PSF size at different points in the accessible volume (Figure 15). The full-width-at-half-maximum (FWHM) values of the PSF in the center of the 20× objective were 470 nm, 490 nm, and 2,490 nm along the x, y, and z axes, respectively (Figure 15a).

DOI:10.15774/PPKE.ITK.2015.003

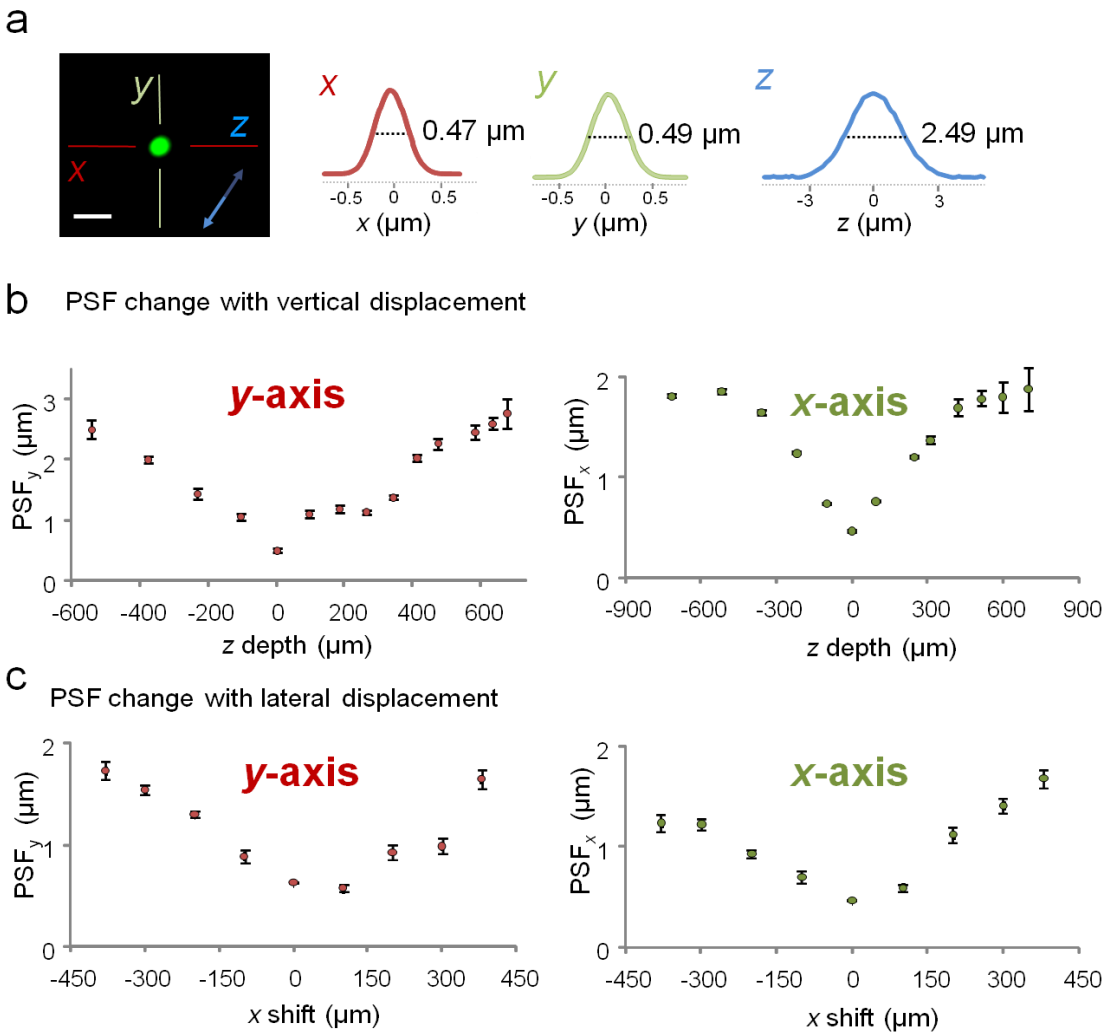

Figure 15 Size of the PSF in the 3D AO scanned volume.

*(**a**) A fluorescent bead (0.1 µm) imaged with the optimized system using the 20× objective in the center (x, y, z) = (0, 0, 0) µm coordinates. (Right) Corresponding intensity profiles along the x, y, z axes with FWHM values. Note radial symmetry in center. Scale bar, 1 µm (**b**) Measured PSF diameters along the x and y axes are plotted as a function of axial AO z-scanning displacement from the nominal object plane of the objective. (**c**) PSF diameters along the x and y axes are plotted as a function of lateral displacement from the optical axis. (Katona et al., 2012)*

Although spatial resolution decreased with radial and axial distances from the center of objective focus (Figure 15b,c), PSF size remained small (diameter <0.8 µm, axial length <3 µm) in the central core of the volume (~290 × 290 × 200 μm^3), allowing the resolution of fine neuronal processes (see later Figure 22a). Moreover, PSF size, being below 1.9 µm diameter and 7.9 µm axial length in an approximately 1,400 µm *z*- and 700 µm lateral-scanning range

DOI:10.15774/PPKE.ITK.2015.003

allowed the optical resolution of individual fluorescent beads (whose radius, 6 µm, is smaller than the average neuronal somata; Figure 16).

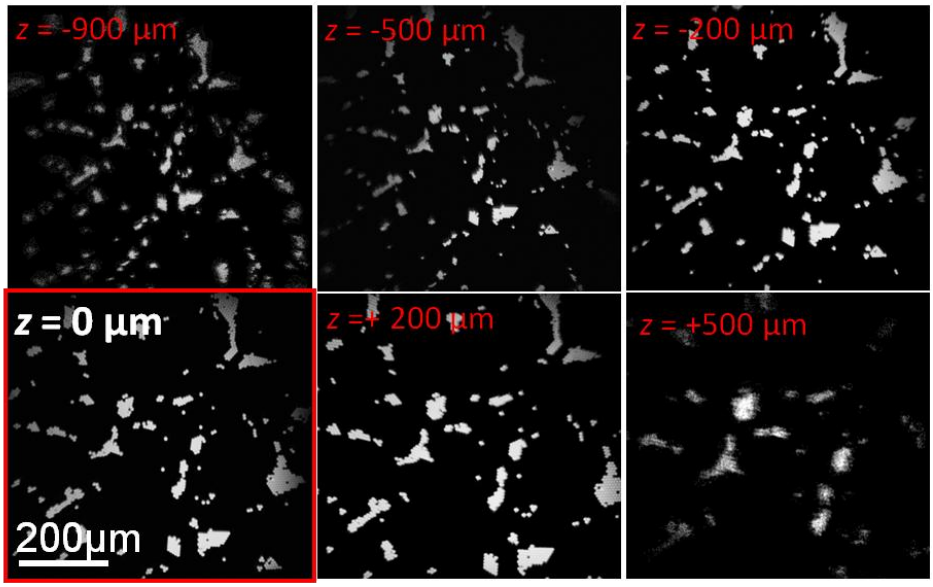

Figure 16 FOV of the microscope system by inspecting fluorescent beads.

The analyzed sample consisted of 6 µm-diameter fluorescent beads on a cover glass. AO z-focusing was compensated for by refocusing the objective mechanically to keep the fixed sample in focus. The inscriptions show objective shifts along the z-axis required for refocusing. The maximal field of view of the system was approximately 700 µm at z = 0 µm. z = 0 was defined as the nominal object plane. Lateral displacement of the field of view, and changes in magnification as a function of AO z-focusing was compensated for in the acquisition program. Individual beads remained visible in a 1400 µm scanning range. (Katona et al., 2012)

With the help of our specially built AO driver electronics featuring frequency dependent amplitude modulation we could also compensate for the diffraction efficiency inhomogeneities of the AO deflectors and also, partially, the drop of intensity at the sides of the images (dynamic power compensation; Figure 17, see also 4.3.3). The large aperture of the AO deflectors allowed precise targeting of the center of the focal point with 51 nm and 140 nm accuracy in the whole volume along radial and axial axes, respectively, which is around 10% of the optimal PSF size.

DOI:10.15774/PPKE.ITK.2015.003

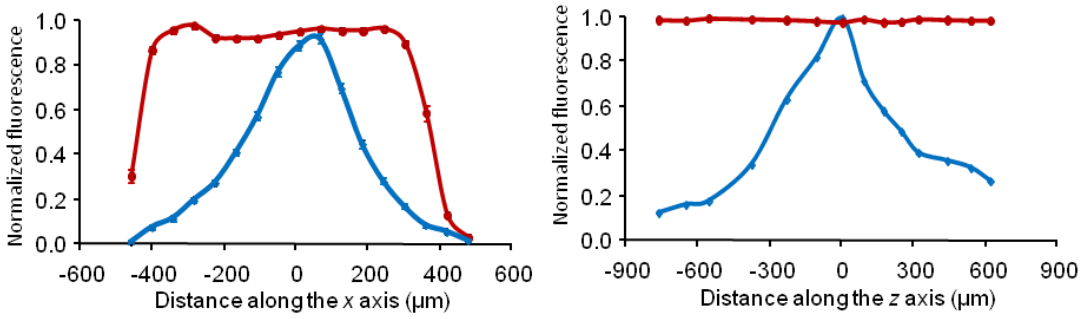

Figure 17 Maximal FOV of the microscope with dynamic power compensation.

Normalized fluorescence intensity of a homogeneous fluorescent sample as a function of distance from the origin along the x *and* z *axes with (red) and without (blue) dynamic power compensation. The uncompensated fluorescence intensity is affected by the variations in both the excitation intensity and the PSF size (blue). We compensated for these technical shortcomings in the driving signals by applying frequency dependent signal amplitude which function was determined in advance (dynamic power compensation; red). (Katona et al., 2012)*

4.5 Testing the 3D AO microscope in vitro and in vivo

In the next step we tested how these parameters can be exploited in biological measurements.

4.5.1 3D random-access scanning of action potential propagation

To examine the temporal resolution of our system we chose imaging one of the fastest events in the brain, APs. We measured propagating activity at seventy-seven 3D locations in a single hippocampal neuron in an acute mouse brain slice. We patch-clamped a CA1 pyramidal cell in whole-cell mode and filled the cell with the green fluorescent Ca^{2+} sensor fluo-5F (Life technologies) and the red fluorescent marker Alexa Fluor 594 (Life technologies). The objective was positioned at the center of the region of interest, fixed, and a reference *z*-stack of images was acquired using 3D AO scanning only (Figure 18). We selected points along the dendritic tree of the patched neuron using either a 3D virtual environment (Figure 13, Katona et al., 2012) or by scrolling through the *z*-stack in a 2D virtual environment (Katona et al., 2011). The cell was held in current-clamp mode and an AP was evoked by somatic current injection while near-simultaneously measuring dendritic

DOI:10.15774/PPKE.ITK.2015.003

Ca^{2+} signals by repetitively scanning the selected 3D coordinates at 29.76 kHz (Figure 18). When sample drift occurred, we repositioned single points or the entire group manually.

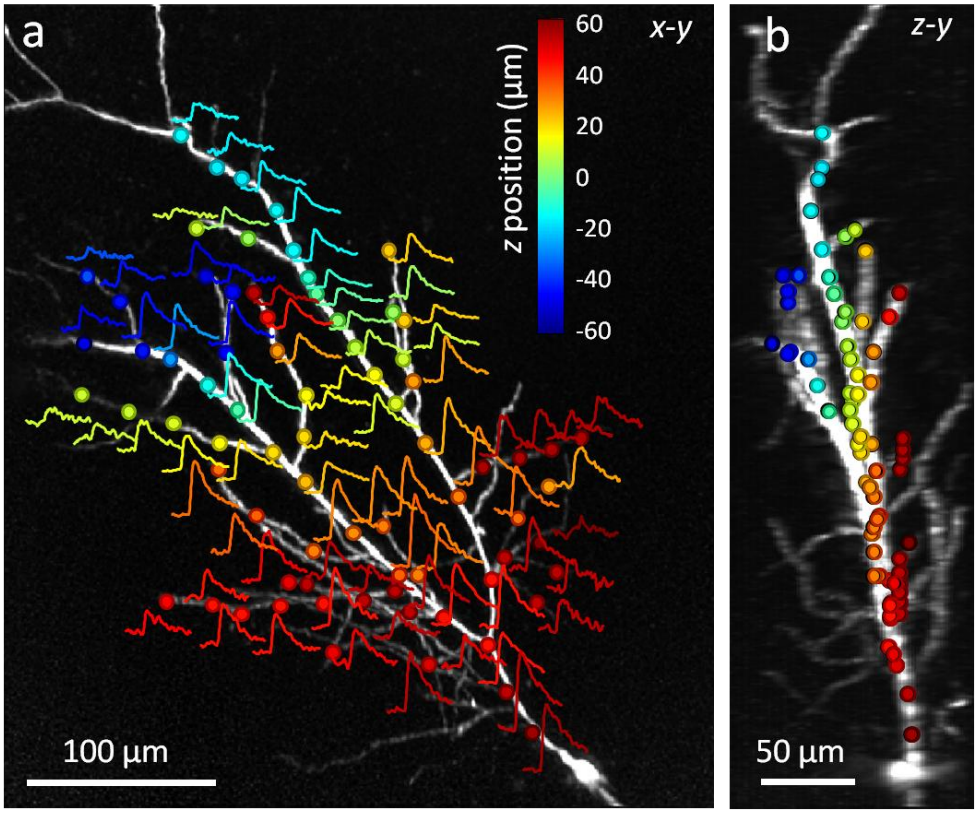

Figure 18 Three-dimensional measurement of bAPs.

*(**a**) Maximum intensity z-projection of the dendritic arbor of a CA1 pyramidal cell imaged by 3D AO scanning. Circles represent the 77 pre-selected measurement locations for 3D random-access point-scanning. Overlaid curves show Ca^{2+} transients recorded near-simultaneously in each location induced by a single bAP (each is the average of five traces). The repetition rate of the measurement was 29.76 kHz (0.39 kHz speed in each location). The z-coordinates of the measurement locations are color-coded. (**b**) Maximum intensity side projection of the cell with the measurement locations shown in **a**. (Katona et al., 2012)*

Since the acute brain slices were 300 µm thick, only a fraction of the total AO *z*-scanning range can be used. To test whether our random-access 3D AO scanning can record bAP-induced Ca^{2+} transients (see 4.8 Materials and methods) we moved the objective focal plane mechanically from +562 µm to −546 µm away from the *z*-center, then used AO *z*-focusing to refocus the recorded dendritic location (Figure 19a). Independent of the AO *z*-settings, single bAPs could be resolved in Ca^{2+} transients induced by a train of three APs. Similarly,

DOI:10.15774/PPKE.ITK.2015.003

single bAPs could be followed in a 760 µm lateral scanning range (Figure 19b). Thus a total of 1190 µm AO *z*-focusing range and a 760 µm AO lateral scanning range is shown with the 20× objective where single APs can be resolved with SNR greater than 1 (Figure 20). This *z*-range was extended over 2000 µm with the use of a 16× objective (Figure 19c). In summary, resolving of single AP-induced transients is possible in a near-cubic-millimeter scanning volume.

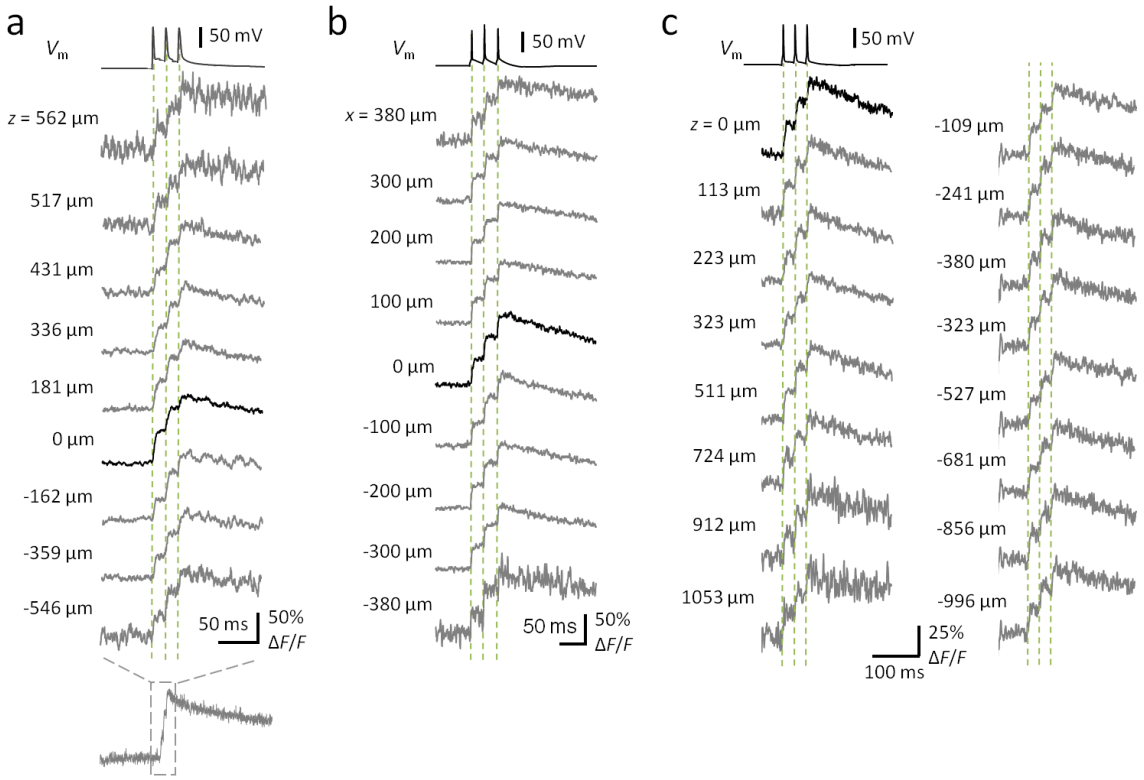

Figure 19 Resolving bAPs at the sides of the FOV.

*(**a**) Single traces of three bAP-induced dendritic Ca^{2+} transients measured at the same dendritic point at different AO z-focusing settings. To keep the sample in focus, the AO z-focusing was compensated by mechanical movement of the objective. Note the preserved single AP resolution even at the lower and upper limits of the scanning range. Corresponding somatic voltage traces (V_m) are shown on the top (**b**) Similarly as in **a**, transients were recorded while shifting the dendrite along the x axis. (**c**) The same as in **a**, but single traces were recorded using the 16× objective. Note that the AO z-focusing range with single AP detection level exceeds 2000 µm. (Katona et al., 2012)*

DOI:10.15774/PPKE.ITK.2015.003

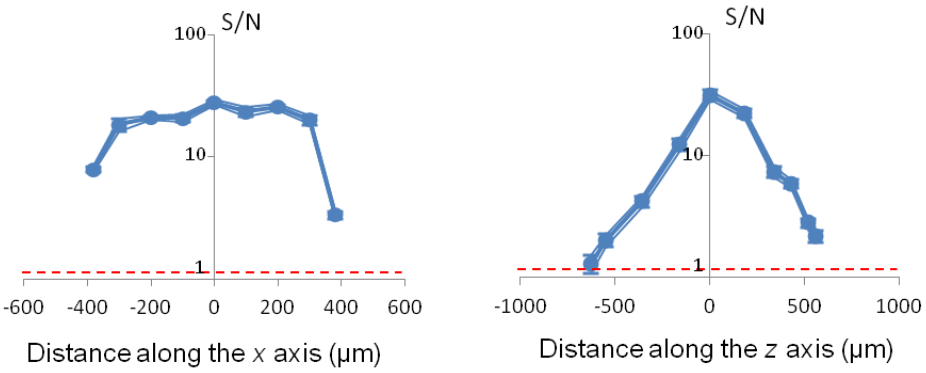

Figure 20 SNR of bAPs in the field of view.

SNR calculated from the pool of transients shown in Figure 19. Peak of the Gauss-filtered bAP-induced Ca^{2+} transients were divided by the standard deviation of the unfiltered 50 ms baseline period (mean ± SEM, n = 10-50 transients at each position). Single AP detection level is marked with a red dashed line. (Katona et al., 2012)

We tested how the temporal resolution of the microscope made possible to measure the propagation speed of bAPs. Similarly to above, a somatic AP was evoked in a pyramidal cell held under current clamp while scanning in 3D along its dendrite. The bAP-evoked Ca^{2+} transients showed increasing latency in dendritic measurements taken further away from the cell body (Figure 21b). The velocity of the bAP was calculated from the latency of the Ca^{2+} transients and the distance from the soma (Figure 21c). Average bAP propagation speed was 164 ± 13 µm/ms (*n* = 9) at 23°C.

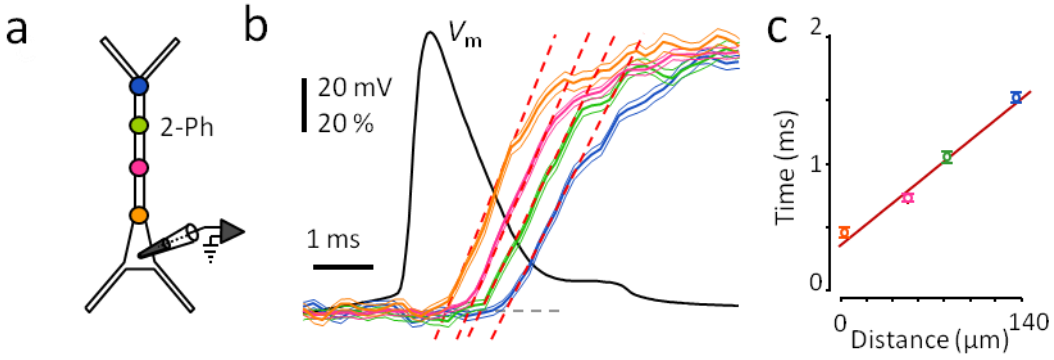

Figure 21 Measurement of bAP propagation speed.

*(**a**) Experimental arrangement for signal propagation experiments. Signal propagation speed was measured by somatic whole-cell current-clamp (Vm, black) and 3D two-photon calcium imaging (orange, pink, green, and blue). (**b**) AP peak triggered average of normalized*

DOI:10.15774/PPKE.ITK.2015.003

*dendritic Ca^{2+} transients induced by bAPs (mean ± SEM; n = 54; top). Linear fits (red dashed lines) define onset latency times. (**c**) Onset latency times (mean ± SEM; n = 54) of Ca^{2+} transients in **b** as a function of dendritic distance. Linear fit: average propagation speed. (Katona et al., 2012)*

Given the importance of integration of activity in the dendrites in neuronal information processing (Johnston and Narayanan, 2008; Losonczy et al., 2008; Spruston, 2008), we tested our system also by recording dendritic spike activity. To investigate the extent and spread of activation, we adapted random-access scanning to measure activity at many discrete points along the 3D trajectory of a dendrite (point-by-point trajectory scanning). As above in section 4.5.1, we scrolled through a reference *z*-stack of a series of pre-recorded images and selected guide points along the length of a dendrite. Then, instead of recording from these manually selected points, we homogeneously re-sampled the trajectory using piecewise cubic Hermite interpolation (Katona et al., 2011). This algorithm is better than conventional spline interpolation because it never overshoots the guide points. The speed of the measurement depended on the number of recording points along the trajectory. In the example shown in Figure 22, we filled a hippocampal CA1 pyramidal cell with Fluo-5F and induced dendritic Ca^{2+} spikes by focal synaptic stimulation with an extracellular electrode at >400 µm from the cell body. We followed the propagating activity optically at uniformly spaced locations along a dendrite (Figure 22a). The recorded traces were normalized by calculating $\Delta F/F$ at each point, and were projected as a function of time and distance measured along the 3D trajectory line (3D Ca^{2+} responses, Figure 22b). The Fluo-5F responses revealed dendritic spikes propagating toward the cell body, both when the stimulation evoked somatic APs (suprathreshold spikes), and when the stimulation was insufficient to evoke somatic APs (subthreshold spikes, Figure 22b-e). After a short initiation phase, subthreshold dendritic spikes propagated rapidly and then gradually ceased before reaching the cell body (Figure 22b). We quantified spike propagation speed by measuring propagation times at the half-maximal amplitude of the transients (Figure 22c) or at the peak of their first derivates (Figure 22d). The average propagation speed was significantly higher for suprathreshold spikes than for subthreshold spikes (subthreshold 81 ± 27 µm/ms, suprathreshold 129 ± 30 µm/ms; 131%, *t*-test, $P = 0.03$; $n = 7$ cells; Figure 22e) and both supra- and subthreshold spikes propagated in the direction of the cell body under these

DOI:10.15774/PPKE.ITK.2015.003

conditions (Figure 22e). Note that despite the large total scanning volume (290 × 290 × 200 μm^3) two-photon resolution was preserved (in the range of 0.45-0.75 µm). The total number of measured points along any given trajectory was 23.8-54.3 points per kHz.

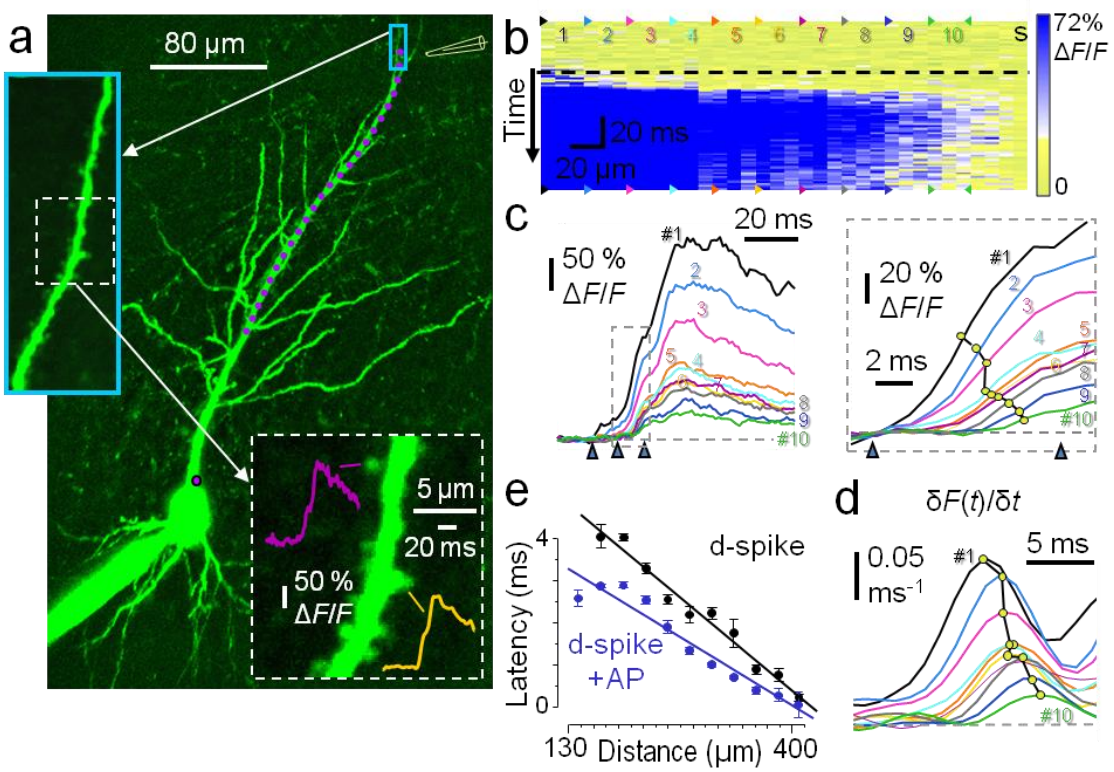

Figure 22 3D scanning of dendritic Ca^{2+} spike propagation in CA1 pyramidal cells.

*(**a**) Maximum-intensity projection of a CA1 pyramidal cell. Ca^{2+} transients in dendritic spines (orange and magenta traces) following induction of dendritic Ca^{2+} spike by focal extracellular stimulation (electrode: yellow). Left and bottom insets, enlarged views. Purple dots represent scanning points in the dendrite. (**b**) Spatially normalized and projected Ca^{2+} signal in the dotted dendritic region shown in a (average of five subthreshold responses). Black dashed line, stimulus onset. Column s, somatic Ca^{2+} response. (**c**) Ca^{2+} transients derived from the color-coded regions indicated in **b**. Right, Baseline-shifted Ca^{2+} transients measured in the region contained in the dashed box in **c**. Yellow dots, onset latency times at the half-maximum. (**d**) Onset latency times at the peak of the derivate (δF(t)/δt) of Ca^{2+} transients shown in **c**. (**e**) Onset latency times as a function of dendritic distance from the soma for somatic subthreshold (black) and suprathreshold (blue) dendritic Ca^{2+} spikes. (Katona et al., 2012)*

DOI:10.15774/PPKE.ITK.2015.003

4.5.2 High-speed *in vivo* 3D imaging of neuronal network activity

To test the performance of our imaging system *in vivo*, we recorded Ca^{2+} responses from a population of individual neurons in the visual cortex of adult anesthetized mice. We injected a mixture of OGB-1-AM to monitor changes in intracellular Ca^{2+} concentrations, and sulforhodamine-101 (SR-101) (Nimmerjahn et al., 2004) to selectively label glial cells (green and red, respectively) (Figure 23). The red fluorescence of SR-101 allowed differentiation between neurons and glial cells. The maximal power of our laser (3.5 W) limited the depth of the *in vivo* recording to a maximum of 500 µm from the surface of the cortex (the total imaging volume was 400×400×500 µm).

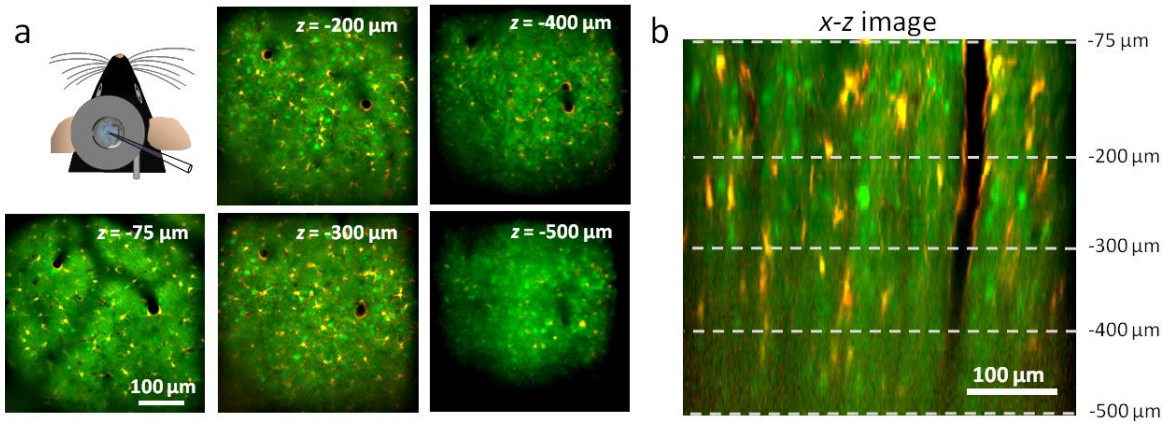

Figure 23 In vivo image stacks of the neuronal population.

*(**a**) Representative background-corrected images taken at different depths from the surface of the brain showing neurons (green) and glial cells (red and yellow). (Upper left) Sketch of in vivo experimental arrangement. Staining by bolus loading (OGB-1-AM and SR-101) in mouse V1. (**b**) x-z slice taken from the middle of the stack volume. Dotted lines correspond to the planes in **a**. (Katona et al., 2012)*

Next, we recorded a reference *z*-stack and, using an automated algorithm, identified neuron and glial cell bodies. When OGB1-AM and SR-101 dyes are bolus-loaded into the animal, cells can be categorized according to their dye content, measured by fluorescence. Neuronal cells can be detected because of their elevated green fluorescence and decreased red fluorescence (Figure 24a). We normalize green and red fluorescent channel data of each image in the stack and then scale and shift so that its 10th and 90th percentiles match 0 and 1. Background correction is done by over-smoothing an image and subtracting it from the

DOI:10.15774/PPKE.ITK.2015.003

original. Next, we subtract the red channel data from the green and each layer of the stack is filtered again (2D Gaussian, σ = 2 µm, Figure 24a bottom). The resulting stack is then searched for local maxima, with an adaptive threshold. If two selected locations are closer than a given distance threshold, only one is kept. At the end the algorithm lists the 3D coordinates of the centers of each neuronal cell body, and these coordinates can be used for random-access activity imaging (Figure 24b).

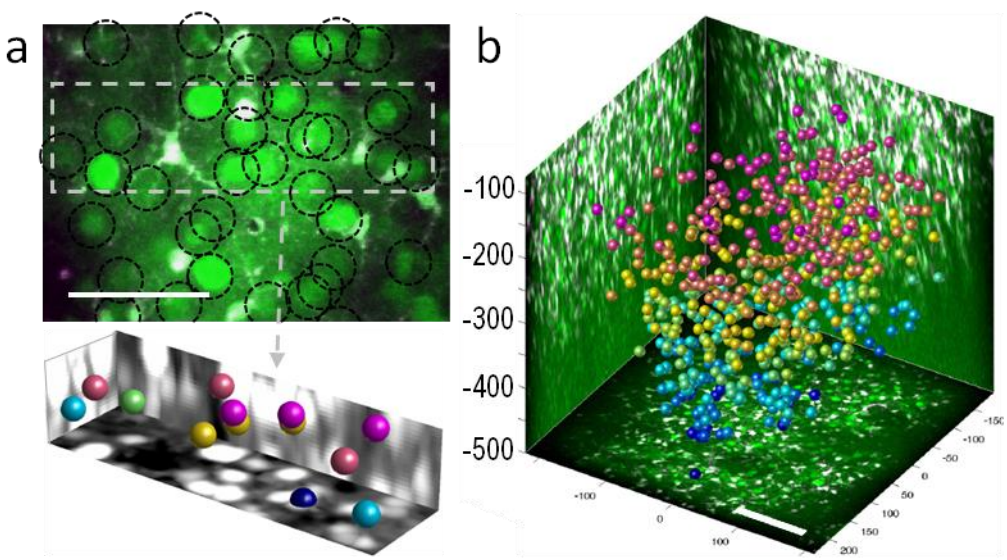

Figure 24 Automatic localization of neurons in vivo.

*(**a**) 35 µm z-projection of a smaller region of the experiment shown also in Figure 23. Bottom, neuronal somata detected with the aid of an algorithm in a sub-volume (shown with projections, neurons in white and glial cells in black). Scale bar, 50 µm. (**b**) Maximal intensity side- and z-projections of the entire z-stack (400×400×500 µm^3) with autodetected cell locations. Spheres are color-coded in relation to depth. The detection threshold used here yielded 532 neurons. Scale bar, 100 µm. (Katona et al., 2012)*

After the cell bodies have been selected (Figure 24, Figure 25b), we first recorded the spontaneous activity of each neuron by scanning at 80 Hz and plotted the point-by-point background-corrected and normalized fluorescence data (Figure 25c), each row showing the activity of a single cell. Responses of neurons could be resolved with SNR (signal amplitude divided by the standard deviation of the noise) being in the range of 7-28. (Figure 25d). The stability of long-term recording was monitored using the baseline fluorescence.

DOI:10.15774/PPKE.ITK.2015.003

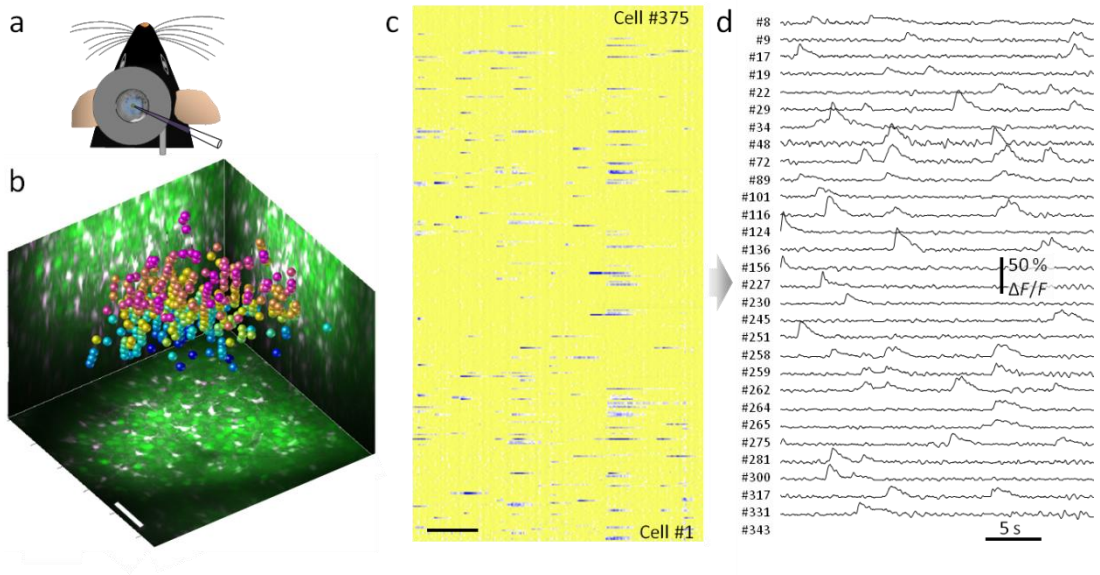

Figure 25 Spontaneous neuronal network activity in vivo.

*(**a**) Sketch of in vivo experimental arrangement. (**b**) Maximal intensity side- and z-projection image of the entire z-stack (280×280×230 µm^3; bolus loading with OGB-1-AM and SR-101). Spheres represent 375 autodetected neuronal locations color-coded by depth. Scale bars, 50 µm. (**c**) Parallel 3D recording of spontaneous Ca^{2+} responses from the 375 locations. Rows, single cells measured in random-access scanning mode. Scale bar, 5 s. (**d**) Examples of Ca^{2+} transients showing active neurons from **c**. (Katona et al., 2012)*

Next, we presented the mouse with visual stimuli (for details see 4.8 Materials and methods section) consisting of movies of a white bar oriented at eight different angles always moving in a direction perpendicular to its orientation (Figure 26a). Visual stimulation with bars oriented at −45° to vertical activated a small subpopulation of the measured cells (Figure 26b,c).

DOI:10.15774/PPKE.ITK.2015.003

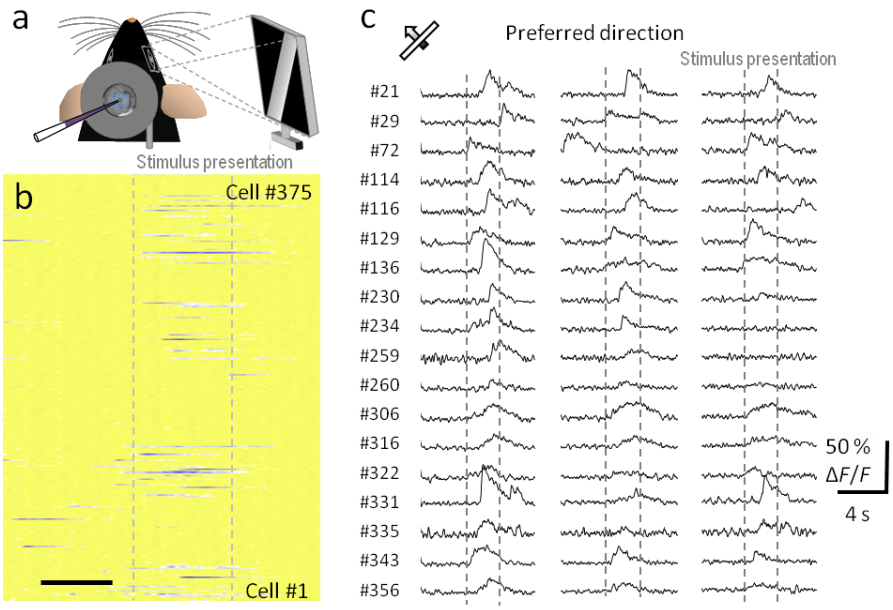

Figure 26 V1 cortical neuronal network activity in vivo in response to visual stimuli.

*(**a**) Sketch of in vivo experimental arrangement. (**b**) Ca^{2+} responses from the same 375 neuronal locations visible in Figure 25 (visual stimulation: moving bar at −45°). Rows, single cells from a single 3D measurement. Scale bar, 2 s. (**c**) Three repeats of measurement, Ca^{2+} transients from neurons responsive in **b**, thus preferentially responding to the −45° bar direction. Bar moved in the visual field during the time periods marked with dashed lines. (Katona et al., 2012)*

We then compared the responses of the 375 individual cells to bars moving in eight different directions (a total 28,125 Ca^{2+} transients were recorded) and found orientation-selective, direction-selective, and orientation-non-selective cells within the full neuronal population measured simultaneously in 3D (Figure 27).

DOI:10.15774/PPKE.ITK.2015.003

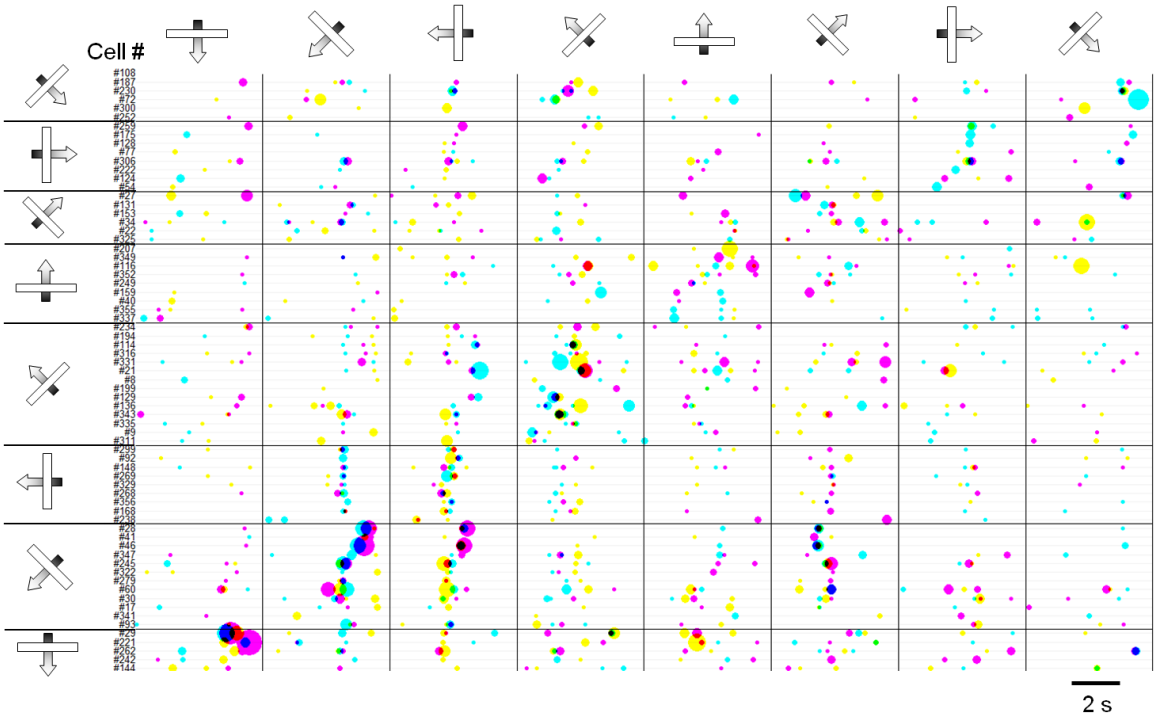

Figure 27 Analysis of V1 cortical neuronal population activity.

Raster plot of the activity of 69 responding neurons from the 375 neurons measured in one sequence with respect to eight different directions of stimulation; the three repeats are color coded. Circle size corresponds to the amplitude of the Ca^{2+} traces. Cells are sorted according to their stimulus preference and response onset. Note the high variability between repeats, asymmetry in the strengths and number of responses to different directions, and the occurrence of similar patterns in response to different directions. (Katona et al., 2012)

4.6 Discussion

We developed a 3D two-photon microscope able to scan a large scanning volume (up to 700 × 700 × 1,400 μm^3), with a high scanning speed of up to 54.3 points/kHz, with 470 × 490 × 2,490 nm^3 resolution in the center core, and less than 1.9 x 1.9 x 7.9 μm^3 resolution throughout the whole scanning volume**.** The maximal addressable volume is an order of magnitude larger than recently achieved by others (Cotton et al., 2013; Fernandez-Alfonso et al., 2014); while we could also use the microscope the first time for 3D random access measurement of neuronal networks *in vivo*.

The improved performance of the microscope presented here can be explained by a number of factors: the different effects are summarized in Figure 28. Detailed, diffraction-based

DOI:10.15774/PPKE.ITK.2015.003

optical modeling predicted an optimal arrangement of passive and active optical elements that were selected from a number of combinations. In contrast to previous arrangements, the four AO deflectors were not grouped together in the most compact arrangement (Kirkby et al., 2010), nor were they separated with relay lenses (Duemani Reddy et al., 2008). Rather, they were grouped into two functionally different subunits in order to increase the lateral FOV of scanning. The first AO pair is used for *z*-focusing, whereas random-access positioning in the *x*-*y* plane was restricted only to the second group of deflectors (2D-AO scanning unit). This arrangement increased the diameter of the lateral scanning range by a factor of ~2.7 (Figure 28a). In addition, not only deflector driver signals, but also deflector geometry, manufacturing, bandwidth, and TeO_2 orientation differ between deflectors of the two groups. According to Figure 28a, FOV was predominantly increased due to the separation of deflectors into two groups, the use of dynamic power compensation and the use of the properly illuminated large aperture objectives.

In contrast to previous realizations of AO scanning (Duemani Reddy et al., 2008; Kirkby et al., 2010), we dynamically compensated for optical errors (astigmatism, field curvature, angular dispersion, chromatic aberration) during measurements. We added corrections to the AO deflector driver functions at each imaged point: this increased spatial resolution in the whole scanning volume (Figure 28b). Dynamic error compensation also allows compensation for focal spot displacement (and optical errors) at a wide range of laser light wavelengths. Therefore, simultaneous two-photon imaging and optogenetic perturbation, or two-photon imaging combined with two-photon uncaging (Katona et al., 2011; Chiovini et al., 2014) may become possible in 3D in the future.

Furthermore, spatial resolution in the whole scanning volume is also increased by the large optical apertures used throughout the system, and ~20% of this increase is due solely to the use of large AO deflector apertures (Figure 28b). In contrast to the dominantly *z*-focusing-dependent effect of dynamic error compensation (spatial resolution increased at $z \neq 0$ planes by a factor of ~2-3), the angular dispersion compensation unit decreases PSF in off-axis positions when compared with a simple two-lens telecentric projection. These factors which decrease PSF also inherently increase the lateral field of view.

DOI:10.15774/PPKE.ITK.2015.003

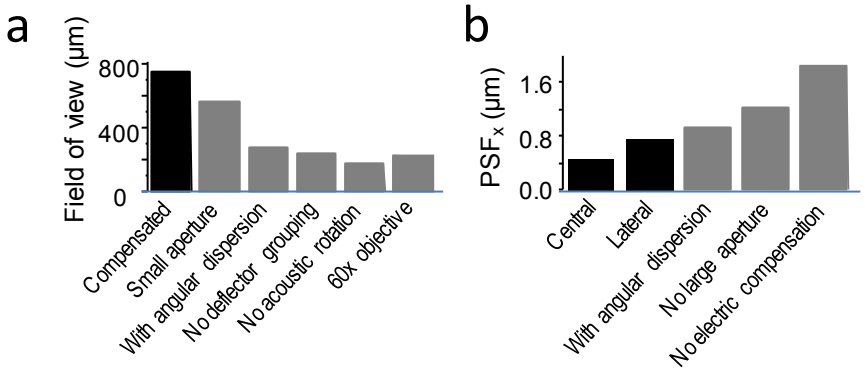

Figure 28 Overview of the effect of enhancements implemented in the setup.

*(**a**) The maximal field of view (compensated) is shown when: both deflector pairs were used for deflection (no deflector grouping) or when optically rotated deflectors (no acoustic rotation), small aperture objectives (60×), no angular dispersion compensation (with angular dispersion) or small aperture AO deflectors were used (small aperture). (**b**) The compensated PSF size along the* x*-axis (*PSF_x*) (central) at (*x, y, z*) = (150, 150, 100) µm coordinates (lateral) or when no angular dispersion compensation (with angular dispersion), no electronic compensation (no electric compensation) or reduced AO apertures were applied (no large apertures). (Katona et al., 2012)*

In order to test the microscope in biological measurements, we performed various measurements both *in vitro* and *in vivo.* First, we measured the SNR of APs at various points in the FOV. Than to test random access scanning, we monitored AP backpropagation at many randomly chosen locations along the dendritic tree of a single neuron. To measure dendritic spikes we used the point-by-point trajectory scanning to monitor multiple locations along a trajectory. Finally, we have shown *in vivo* random access 3D measurements the first time by sampling the activity of hundreds of neurons in the V1 cortical area of a living mouse while presenting visual stimulation.

4.7 Future perspectives

Understanding the functioning of the brain gains focus in the recent years with the emergence of new technologies speeding up this global journey. We have discussed that two-photon microscopy is the best tool to study brain function down to the cellular levels in relatively intact tissues or even in living animals. We have shown a 3D AO microscope

DOI:10.15774/PPKE.ITK.2015.003

offering the fastest and most flexible inertia free means of 3D positioning of the focal spot to the regions of interest.

Optically, 3D AO microscopes are now close to the theoretical maximum which can be realized using the currently available objective lenses, but other aspects of AO scanning could still be improved, such as

- develop faster, more specialized scanning algorithms for network measurements
- develop faster AO deflectors
- increase speed of the electronics to compete resonant frame scanning
- develop novel correction methods for movement artifacts
- improve lasers and fluorescent dyes to get access to entire thickness of the cortex
- applying the technology to larger FOV objectives
- implement adaptive optics
- simplify the system to lower its costs and maintenance efforts
- improve wavelength tunability

Together with these developments we would like to extend the system to be able to scan at multiple brain areas simultaneously in order to study communication between sensory, motor and higher order areas and to incorporate photostimulation features during 3D scanning for it to be possible to functionally map connectivity within neuronal networks.

I hope that this technology will gain a significant share among the tools used to study brain function, and adds a new view to the sight of neuroscience which I believe will be significantly influencing our technology and lives by the end of this century.

4.8 Materials and methods

Animals. Male or female C57Bl/6J wild-type mice or Wistar rats were kept under a 12-h day and night cycle with food and water provided ad libitum and were handled in accordance with the Hungarian Act of Animal Care and Experimentation (1998; XXVIII, section 243/1998.). The Animal Care and Experimentation Committee of the Institute of Experimental Medicine of the Hungarian Academy of Sciences and the Animal Health and Food Control Station, Budapest, have approved the experimental design (reference numbers 22.1/4015/003/2009, 18_1/2009 and 19_1/2009).

DOI:10.15774/PPKE.ITK.2015.003

Slice preparation and electrophysiology. Acute hippocampal slices were prepared from P16-20 Wistar rats or P16-26 C57Bl6/J mice using isoflurane anesthesia followed by swift decapitation, in accordance with the Hungarian Act of Animal Care and Experimentation (1998; XXVIII, section 243/1998.). Horizontal (300-400 µm) brain slices were cut with a vibratome and stored at room temperature in artificial cerebrospinal fluid (ACSF) (in mM: 126 NaCl, 2.5 KCl, 2 $CaCl_2$, 2 $MgCl_2$, 1.25 NaH_2PO_4, 26 $NaHCO_3$, and 10 glucose) as previously described (Rozsa et al., 2004; Rozsa et al., 2008; Katona et al., 2011; Katona et al., 2012).

Cells in the CA1 area of the hippocampus were visualized using 900 nm infrared lateral illumination (Rozsa et al., 2008). Current-clamp recordings were made at 23°C and 33°C (MultiClamp 700B, Digidata 1440: Molecular Devices; chamber heater: Luigs & Neumann; in-line heater: Supertech). For whole-cell current-clamp recordings, glass electrodes (6-9 MΩ) were filled with (in mM): 125 K-gluconate, 20 KCl, 10 HEPES, 10 Di-Tris-salt phosphocreatine, 0.3 Na-GTP, 4 Mg-ATP, 10 NaCl, and 0.1 Oregon Green BAPTA-1 (OGB-1, Invitrogen). In propagation speed measurements, 0.2 Fluo-5F pentapotassium salt (Invitrogen) and 0.04 Alexa594 (Invitrogen) were used instead of OGB-1. bAPs were induced by somatic current injections (200-400 pA, 5 ms; 1-3 bAPs were evoked at 50 Hz). All chemicals and drugs, unless otherwise noted, were purchased from Sigma. Cells with a resting membrane potential more negative than –50 mV were accepted. Two-photon imaging started 15–20 min after attaining the whole-cell configuration

Focal synaptic stimulation was performed as described previously (Rozsa et al., 2004; Rozsa et al., 2008; Katona et al., 2011; Katona et al., 2012). Briefly, 6-9 MΩ glass electrodes filled with ACSF were placed at a distance of 10-15 µm from the dendrite (stimulation: 0.1 ms, 10-50 V, 10 ms pulse interval, 1-3 stimuli; BioStim, Supertech). Electrodes were targeted to the dendrite by a program written in MATLAB synchronizing the coordinate system of the patch-clamp manipulator and the microscope by the simultaneous use of two-photon imaging and transmitted oblique laser light data. All evoked EPSPs were verified for synaptic delay.

***In vivo* bolus loading.** Male or female C57Bl/6J wild type mice (P 60-130) were kept under a 12-hour day and night cycle with food and water provided ad libitum and were handled in accordance with the Hungarian Act of Animal Care and Experimentation (1998; XXVIII, section 243/1998.) The procedure for surgery and *in vivo* bolus loading was performed as previously described (Stosiek et al., 2003). Briefly, mice were sedated with isoflurane and

DOI:10.15774/PPKE.ITK.2015.003

anaesthetized with an injection of chlorprothixene (0.05 mg/kg ip) and urethane (0.75 mg/kg ip). The skull was exposed and a cranial window (3 mm in diameter) was opened above the visual cortex (V1). Bulk loading was performed with a patch pipette using Oregon Green BAPTA-1 AM (2 mM, Invitrogen) and sulforhodamine-101 (200 μM, Invitrogen) under two-photon guidance (810 nm), and a cover glass was fixed to the skull above the cranial window, along with a light-shielding cone. Cell imaging was started 1 h after dye loading to allow for proper staining.

Visual stimulation. A video projector (Acer K10, pixel resolution 856×600) was used to cast the visual stimuli generated by a program written in MATLAB using the 'Psychtoolbox' addon package on a screen placed 20 cm from the contralateral eye (covering ~100° × 70° of the visual field). To prevent stray light from entering the objective, a black cover was placed over the complete projection path. The objective had a separate light shield consisting of a metal cylinder that slid onto the cone fixed to the animal's head. Each trial of the visual stimulation started by showing a black screen with a single white bar appearing at the edge of the screen after 2 s; after 1 s, the bar moved in a direction orthogonal to its orientation for 5 s (drifting speed 1 cycle per 5 s), was stopped for 1s, and then disappeared, leaving a black screen for a further 1 s. Trials with eight different bar directions were tested with an angular interval of 45°.

Optical engineering. The optical system, including dispersion compensating prisms, beam expander, acousto-optic deflectors, telecentric relays, and microscope objectives, was modeled and optimized with OSLO (Lambda Research) and ZEMAX (ZEMAX Development) optical designer programs. Several parameters of the optical system were optimized using built-in and custom optimization algorithms written in MATLAB (MathWorks) and Mathcad (Mathsoft). We selected PSF, focal spot Strehl-ratio (quantification of optical aberrations), and wavefront error for optimization. The operation and configuration of the acousto-optic devices were optimized in a dedicated anisotropic acousto-optic model developed for the acousto-optic interaction and for dedicated acousto-optic devices (see below). After finding the optimal configuration and arrangement of optical elements we continued optimization by replacing components with commercially available optical elements, while keeping the high performance. The acousto-optic devices were modeled by a set of user-defined surfaces in the optical designer programs (ZEMAX) that accounted for anisotropic interaction geometry, chirp effects, and phase shifts with high precision levels. The detailed

DOI:10.15774/PPKE.ITK.2015.003

description of optical wavelength dependence of the interaction in the program accurately modeled angular dispersion.

The lens chain of the optical system was optimized to provide the best optical relay, with minimized optical errors between the consecutive optical units. One design challenge was to provide optimal illumination of the objective lenses to produce minimal diffraction-limited spot size and the highest possible optical resolution within the sample.

Non-sequential calculations were also performed, using custom scattering DLLs to determine power distributions at the sample, mainly within the focal spot. The acousto-optic deflectors were custom-designed for their specific applications in the z-focusing unit and the scanning unit. Their orientation, size, frequency range, and aperture were calculated using custom optimization programs in Mathcad and Matlab.

When the focal plane is electronically shifted and moved away from the optimal focal plane (where the electronic AO lenses are close to their minimum sweep rate), the spot size increases and the Strehl ratio decreases. Modeling confirms that the focal plane shift of −850 µm and +400 µm corresponds to the boundary planes where the Strehl ratio of the focal spot on the objective axis decreases to approximately 0.15, from the original 0.95 (Figure 16 and Figure 17). Here, the lateral optical resolution does not decrease abruptly, because the two-photon effect depends on the square of the intensity density, reducing the size of the spot participating in the excitation, if the total exciting intensity is compensated electronically through the applied acoustic power.

Acousto-optical deflectors. According to modeling results, the two different types of TeO_2 acousto-optic deflectors were custom-designed and manufactured to fit their particular roles. The crystals are custom grown, oriented, and cut for the desired operation. The first type of deflectors, which was used in the AO *z*-focusing unit is set to achieve high (~75%) diffraction efficiency in 40 MHz bandwidth (60-100 MHz) and to lower interaction length (10.5 mm) to minimize dispersion. The acoustic off-axis angle is of 3.5°, for which the acoustic energy walkoff angle (difference angle between acoustic wavefront and energy propagation direction) is ~26°. The rectangular-shaped transducer of 1.6 mm size parallel to the light path is placed 0.5 mm apart from the entrance aperture, so the acoustic beam would propagate transversally more than 16 mm before reaching the output optical aperture facet. However, the deflector crystal is 16 mm long along the acoustic wave vector

DOI:10.15774/PPKE.ITK.2015.003

axis, to avoid reflection of the acoustic beam from the output facet. High bandwidth of the transducer is ensured by electronic matching and the use of a 12 μm thick aluminum layer, acting as an acoustic quarter-wave layer within the transducer layer structure. Lateral scanning of the laser beam is confined to the 2D AO scanner unit. This unit is comprised of deflectors optimized for high bandwidth (55-110 MHz) uniform AO diffraction, with a resolution of 1020 spots (calculated from the T.BW product). The second deflector of the unit was rotated by 90° relative to the first. In contrast to previous realizations[5], both deflectors were purely acoustically rotated in the scanning unit to ensure a symmetrical and large field of view. An optically rotated configuration for a deflector[5] would reduce incidence angle tolerance, which would result in a reduced and asymmetrical FOV. The optical aperture of these cells had a minimum of 17 mm, whereas their length was 30 mm to avoid acoustic reflection from the optical input or output surfaces. This was necessary, since the higher bandwidth of these cells was obtained by larger (4.3°) off-axis acoustic propagation angles than those used in the focusing unit, thus resulting in higher acoustic energy walkoff and device length. These deflectors were built in cooperation with Gooch & Housego. The optical apertures of deflectors of the AO z-focusing unit and the 2D AO scanner unit were 15 mm and 17 mm, respectively, which increased spatial resolution in the whole scanning volume.

The 3D virtual-reality user interface. The 3D virtual-reality user interface was based on Leonar3Do (3DforAll) consisting of shutter glasses, a 3D mouse called “bird”, position sensors, and an LCD display. Briefly, sensors measure the positions of the shutter glasses so that the actual view angle and position of the user’s eyes can be calculated, and the two images corresponding to the left and right eye views can be generated real-time. Views are calculated so that the scene displayed remains in its virtual 3D position (in reference to the LCD display), even if the head position of the user changes. The position of the “bird” was also monitored by the position sensors, and a 3D virtual pointer was added to the image according to the measured coordinates. With the help of the “bird”, users have real-time access to the measurement by selecting or modifying points of 3D trajectory or random access measurements Custom-written software based on the OpenSceneGraph open source high performance 3D graphics toolkit performed the head tracked, GPU-based, real-time visualization of the volumetric data.

DOI:10.15774/PPKE.ITK.2015.003

The 3D AO microscope. Laser pulses are provided by a Mai Tai DeepSee femtosecond laser (SpectraPhysics). The optimal wavelength range is 740 - 880 nm. Pulse back reflection to the laser source is eliminated by a Faraday isolator (BB8-5I, Electro-Optics Technology). Next, the beam position is stabilized using two motorized mirrors (m, AG-M100N, Newport), which stabilizes the position of the light transmitted by two backside custom-polished broad-band mirrors (BB2-E03; Thorlabs) on the surface of two quadrant detectors (q, PDQ80A, Thorlabs). The positioning feedback loop (U12, LabJack Corporation) is controlled by a program written in LabView (National Instruments). The beam is expanded by two achromatic lenses arranged in a Galilean telescope (f = −75 mm, ACN254-075-B, Thorlabs; f = 200 mm, NT47319, Edmund Optics; distance = 125.62 mm) to match the large apertures of the first pair of AO deflectors (15 mm). Mirrors, λ/2 waveplates and holders, are purchased from Thorlabs and Newport. AO deflectors have been custom designed and manufactured at the Budapest University of Technology and Economics. Achromatic telecentric relay lenses were purchased from Edmund Optics (f_{TC} = 150 mm, NT32-886). Achromatic scan and tube lenses were chosen from Edmund Optics (f = 250 mm, NT45-180) and Olympus (f = 210 mm) respectively. The AO-based 3D scanner system is attached to the top of a galvanometer-based upright two-photon microscope (Femto2D-Alba, Femtonics Ltd.) using custom-designed rails. AO sweeps are generated by the direct digital synthesizer chips (AD9910, 1 GSPS, 14-bit, Analog Devices) integrated into the modular electronics system of the microscope using FPGA elements (Xilinx). Red and green fluorescence are separated by a dichroic filter (39 mm, 700dcxru, Chroma Technology) and are collected by GaAsP PMTs custom-modified to efficiently collect scattered photons (H7422P-40-MOD, Hamamatsu), fixed directly onto the objective arm (travelling detector system). In *in vitro* experiments the forward emitted fluorescence can also be collected by 2-inch aperture detectors positioned below the condenser lens (Femto2D-Alba, Femtonics). Signals of the same wavelength measured at the epi- and transfluorescent positions are added. The large aperture objectives, XLUMPlanFI20x/0.95 (Olympus, 20×, NA = 0.95) and CFI75 LWD 16XW (Nikon, 16×, NA = 0.8) provides the largest scanning volume. The maximal output laser power in front of the objective is around 400 mW (at 875 nm).

DOI:10.15774/PPKE.ITK.2015.003

4.9 Thesis

***Thesis 3**: I developed a new technique by using new electronic and software driving algorithms furthermore, specialized measurement and data analysis principles on a 3D scanning AO microscope. The method can collect measurement data in a 700*700*2000 μm^3 volume in transparent samples in random-access mode. I modified the method to be able to measure activity across neuronal networks at high temporal resolution.*

Publication related to the thesis: Rozsa et al., 2007; Katona et al., 2012.; Chiovini et al., 2014.

Our goal was to create a 3D random-access laser scanning two-photon microscope which overcomes mechanical limits posed by earlier solutions. An ideal 3D microscope for neuroscience applications needs to simultaneously satisfy two different needs in the largest possible scanning volume. The first need is to record activity across the dendritic tree of a single neuron at high spatial and temporal resolution in 3D in a way that dendritic spines remain resolvable. The second need is to record in a more extensive volume at high speed in order to capture activities of a large number of cell bodies in a neuronal population.

Several novel technologies have been developed to generate 3D readouts of fast population and dendritic activities; however, in 2012 there were limitations in the use of these methods both *in vitro* and *in vivo*. Acousto-optical (AO) scanning combined with the single-point two-photon ROI scanning approach can penetrate deep in the living tissue and simultaneously increase the measurement speed and the signal-to-noise ratio as compared to classical raster scanning.

In an earlier design we proposed to use optical fibers to achieve 3D random access point scanning and used two AO deflectors to couple light alternating into the fibers (Rozsa et al., 2007). Recent efforts used rather four AO deflectors with which in sequence it is possible to position the focal point in all three dimensions when using synchronized and chirped driving signals.

We created a detailed optical model of the 4 AO deflector sequence. Following the arrangement suggested by the model, a large aperture (15-17 mm) optical assembly was constructed and coupled into a two-photon microscope (Katona et al., 2012). The major difference between the system described here and previous designs is that here the AO

DOI:10.15774/PPKE.ITK.2015.003

deflectors form two functionally and physically different groups. The first AO deflector pair is used for *z*-focusing, whereas random-access positioning in the *x*-*y* plane is restricted only to the second group of deflectors. This arrangement increased the diameter of the lateral scanning range by a factor of about 2.7. Furthermore, not only electronic driver function, but also deflector geometry, TeO_2 crystal orientation and bandwidth are different between deflectors of the two groups. Altogether these factors increased the diameter of the lateral scanning range up to 720 µm using the Olympus 20× objective and over 1100 µm with the Nikon 16× objective. Although spatial resolution decreased with radial and axial distances from the center of objective focus, PSF size remained small (xy <0.8 µm, z <3 µm) in the central core of the volume (approximately 290 × 290 × 200 μm^3), allowing the resolution of fine neuronal processes and remained below 1.9 µm diameter and 7.9 µm axial length in the whole FOV (now over 1100 × 1100 × 3000 μm^3 in transparent samples) allowing the resolution of cell somata.

We created specialized electronics and software to generate driving signals for the AO scanning. The position and the movement of the focal point is determined by eight values. Four of them control the starting acoustic frequency on the four AO deflector drivers, while the other four define the frequency ramp speeds (chirping). By perturbing calculation of these parameters we could dynamically compensate for various optical errors. Finally, all of the eight parameters need to be continuously updated to the syntheser electronics in every sweep cycle (typically 33.6 µs is used) while the photomultipliers of the system are sampled synchronously.

We extended the microscope control software used in the previous chapters and added new measurement modes for *xy* scanning, 3D Multiple Line Scanning and *z*-stack creation using the AO scanner. We also added new cell localization, point handling and trajectory selecting tools supporting the 3D requirements. We also added a 3D virtual reality environment to the system.

To examine the temporal resolution of our system we chose imaging propagating activity of single hippocampal neurons in acute brain slices. We patch-clamped CA1 pyramidal cells in whole-cell mode and filled the cells with the green fluorescent Ca^{2+} sensor Fluo-5F and the red fluorescent marker Alexa 594. The imaged subvolume containing the cell was 700 × 700 × 140 μm^3. Action potentials were evoked by somatic current injection while we could

DOI:10.15774/PPKE.ITK.2015.003

measure dendritic Ca^{2+} signals near-simultaneously at eighty-seven 3D locations selected by the experimenter. In other experiments we were able to measure in fine processes the propagation speed of action potentials or dendritic spikes in an all optical way.

In a recent study we used AO scanning to investigate dendritic spikes on parvalbumin containing interneurons during SPW activity (Chiovini et al., 2014) proving that the AO deflector based 3D scanning methods are indeed usable to address questions unanswerable with other techniques.

To test the performance of our imaging system *in vivo*, we recorded Ca^{2+} responses from a population of individual neurons in the visual cortex of adult anesthetized mice. We injected a mixture of OGB-1-AM to monitor changes in intracellular Ca^{2+} concentrations, and sulforhodamine-101 to selectively label glial cells. The total imaging volume was 400×400×500 µm. First, we recorded a reference *z*-stack and, using an automated algorithm, identified the neuron and glial cell bodies. The algorithm listed 3D coordinates of the centers of each neuronal cell body and these coordinates were used for high speed random-access activity imaging. Next, we presented the mouse with visual stimuli consisting of movies of a moving white bar oriented at eight different angles. We then compared the simultaneously measured responses of the 375 individual cells to the bar's moving direction (a total 28,125 Ca^{2+} transients were recorded) and found orientation-selective, direction-selective, and orientation-non-selective cells within the neuronal population. These experiments showed that AO scanning can perform simultaneous measurement of activity in large 3D neuronal networks *in vivo*, even during complex measurement scenarios.

DOI:10.15774/PPKE.ITK.2015.003

5 SUMMARY

Two-photon microscopy is the ideal tool to study how signals are processed in the functional brain tissue. However, its early raster scanning strategy was inadequate to record fast events like action potentials especially not in 3D. Our aim was to develop new laser scanning strategies and during the years we made three steps forward in the development of new scanning methods for fast neurophysiology measurements.

Multiple Line Scanning enables the experimenter to select multiple regions of interests – although only in two dimensions – and focus the measurement only to them. Doing this not only increases repetition speed, but also signal-to-noise ratio of the fluorescence transients (Lorincz et al., 2007).

As the next step, Roller Coaster Scanning was our first approach to reach fast three dimensional scanning and is appropriate to scan 3D trajectories of tortuous dendrites thereby enabling longer processes to be imaged in one measurement (Katona et al., 2011).

Finally, we developed an acousto-optical deflector based 3D scanning microscope with a millimeter *z*-scanning range and sub-millisecond temporal resolution. Its use for single neuron imaging *in vitro* is demonstrated by obtaining 3D optical recordings of action potential backpropagation, as well as dendritic Ca^{2+} spike forward propagation in several hundred micrometers long neuronal processes. Its use for imaging neuronal populations *in vivo* is shown by 3D random-access scanning of Ca^{2+} transients in hundreds of neurons in the mouse visual cortex (Katona et al., 2012).

To compare these three methods, parameters have been summarized in Table 1.

	Thesis 1 Multiple Line Scanning with galvanomotors	***Thesis 2 Roller Coaster Scanning***	***Thesis 3 3D acousto-optic scanning***
Optical resolution (center of FOV;20x)	450 nm in XY and 2400 nm in Z	450 nm in XY and 2400 nm in Z	470 nm in XY and 2490 nm in Z
Field of view (20x)	*650* µm	*650* µm	*600* µm

DOI:10.15774/PPKE.ITK.2015.003

	Thesis 1 Multiple Line Scanning with galvanomotors	*Thesis 2 Roller Coaster Scanning*	*Thesis 3 3D acousto-optic scanning*
Z scanning range	*0* µm	*Depends on repetition rate.* *28* µm @ 150 Hz *80* µm @ 10 Hz	*Limited by penetration depth* *2000* µm in transparent sample 500 µm *in vivo*
Maximum scanning speed	*2 kHz on a short straight line*	*200 Hz*	*15 kHz on two points arbitrary selected*
Minimum dwell time	*0.1 µs electronics limits*	*0.1 µs electronics limits*	*10 µs crystals limit*
Scan pattern limitations	*Arbitrary 2D curves, straight or curved ROI segments, point scans. Only in 2D.*	*Closed 3D trajectory having one monotone up going and one monotone down going part.*	*Arbitrary 3D curves, straight or curved ROI segments, 3D point scans.*
Small distance step time	*10 µs*	*trajectory limits*	*10 µs*
Large distance step time	*120 µs*	*trajectory limits*	*10 µs*
SNR gain over raster scanning	*typically 3-4; theoretically up to 29*	*trajectory limits*	*typically 50 at neuronal network; theoretically up to 25000*
Wavelength range	*> 400 nm Objective limits*	*> 400 nm Objective limits*	*Fixed wavelength within 700-900 nm*
Scanning of neuron processes	*Various patterns in 2D*	*3D scanning with limitations*	*Various patterns in 3D*
Scanning of neuron networks	*200 µs / cell. Only in 2D*	*Up to about 20 cells in 3D. Limitations on the distribution of cells.*	*30 µs / cell, 3D Up to 2000 cells has been shown in vivo,*
Price of a system	*~ 150 000 EUR*	*~ 200 000 EUR*	*~ 500 000 EUR*

Table 1: Comparison of scanning methods

2D galvanometric scanning is a simple, relatively cheap, still flexible solution, very much suited for in vitro cellular studies. Roller Coaster scanning poses limits on the trajectory selection, however, using the same hardware it is also possible to raster scan on planes not parallel with the focal plane and to perform 4D (XYZT) raster scanning which is useful at certain measurements. The AO microscope is expensive due to its complex optics. It poses for the same reason limits on the laser wavelength, whereas the other two systems allow using

DOI:10.15774/PPKE.ITK.2015.003

a wide wavelength range without adjusting the optics. Still, 3D AO scanning is clearly superior according to the flexibility of possible scanning patterns, it can perform all scanning scenarios the two other systems are able to and it can do 3D random access point scanning which is necessary to optically perform activity measurements in (3D) neural networks.

DOI:10.15774/PPKE.ITK.2015.003

REFERENCES

Cumulative impact factor: 98,5

References by the autor related to the topic

Katona G, Kaszas A, Turi GF, Hajos N, Tamas G, Vizi ES, Rozsa B (2011) Roller Coaster Scanning reveals spontaneous triggering of dendritic spikes in CA1 interneurons. Proc Natl Acad Sci U S A 108:2148-2153

Katona G, Szalay G, Maak P, Kaszas A, Veress M, Hillier D, Chiovini B, Vizi ES, Roska B, Rozsa B (2012) Fast two-photon in vivo imaging with three-dimensional random-access scanning in large tissue volumes. Nat Methods 9:201-208.

Lorincz A, Rozsa B, Katona G, Vizi ES, Tamas G (2007) Differential distribution of NCX1 contributes to spine-dendrite compartmentalization in CA1 pyramidal cells. Proc Natl Acad Sci U S A 104:1033-1038. A. Lorincz and B. Rozsa contributed equally to this work.

Rozsa B, Katona G, Vizi ES, Varallyay Z, Saghy A, Valenta L, Maak P, Fekete J, Banyasz A, Szipocs R (2007) Random access three-dimensional two-photon microscopy. Appl Opt 46:1860-1865.

Other references by the author

Beke D, Szekrenyes Z, Palfi D, Rona G, Balogh I, Maak PA, Katona G, Czigany Z, Kamaras K, Rozsa B, Buday L, Vertessy B, Gali A (2013) Silicon carbide quantum dots for bioimaging. Journal of Materials Research 28:205--209.

Chiovini B, Turi GF, Katona G, Kaszas A, Erdelyi F, Szabo G, Monyer H, Csakanyi A, Vizi ES, Rozsa B (2010) Enhanced dendritic action potential backpropagation in parvalbumin-positive basket cells during sharp wave activity. Neurochemical research 35:2086-2095.

Chiovini B, Turi GF, Katona G, Kaszas A, Palfi D, Maak P, Szalay G, Szabo MF, Szabo G, Szadai Z, Kali S, Rozsa B (2014) Dendritic spikes induce ripples in parvalbumin interneurons during hippocampal sharp waves. Neuron 82:908-924.

Holderith N, Lorincz A, Katona G, Rozsa B, Kulik A, Watanabe M, Nusser Z (2012) Release probability of hippocampal glutamatergic terminals scales with the size of the active zone. Nat Neurosci 15:988-997.

Rozsa B, Katona G, Kaszas A, Szipocs R, Vizi ES (2008) Dendritic nicotinic receptors modulate backpropagating action potentials and long-term plasticity of interneurons. Eur J Neurosci 27:364-377.

Tonnesen J, Katona G, Rozsa B, Nagerl UV (2014) Spine neck plasticity regulates compartmentalization of synapses. Nat Neurosci 17:678-685.

DOI:10.15774/PPKE.ITK.2015.003

Independent references

Amos WB, White JG, Fordham M (1987) Use of confocal imaging in the study of biological structures. Appl Opt 26:3239-3243.

Ariav G, Polsky A, Schiller J (2003) Submillisecond precision of the input-output transformation function mediated by fast sodium dendritic spikes in basal dendrites of CA1 pyramidal neurons. J Neurosci 23:7750-7758.

Betzig E, Patterson GH, Sougrat R, Lindwasser OW, Olenych S, Bonifacino JS, Davidson MW, Lippincott-Schwartz J, Hess HF (2006) Imaging intracellular fluorescent proteins at nanometer resolution. Science 313:1642-1645.

Botcherby EJ, Smith CW, Kohl MM, Debarre D, Booth MJ, Juskaitis R, Paulsen O, Wilson T (2012) Aberration-free three-dimensional multiphoton imaging of neuronal activity at kHz rates. Proc Natl Acad Sci U S A 109:2919-2924.

Cheng A, Goncalves JT, Golshani P, Arisaka K, Portera-Cailliau C (2011) Simultaneous two-photon calcium imaging at different depths with spatiotemporal multiplexing. Nat Methods 8:139-142.

Cotton RJ, Froudarakis E, Storer P, Saggau P, Tolias AS (2013) Three-dimensional mapping of microcircuit correlation structure. Front Neural Circuits 7:151.

Danilatos GD (1991) Review and outline of environmental SEM at present. Journal of microscopy 162:391-402.

Denk W, Svoboda K (1997) Photon upmanship: why multiphoton imaging is more than a gimmick. Neuron 18:351-357.

Denk W, Strickler JH, Webb WW (1990) Two-photon laser scanning fluorescence microscopy. Science 248:73-76.

Duemani Reddy G, Kelleher K, Fink R, Saggau P (2008) Three-dimensional random access multiphoton microscopy for functional imaging of neuronal activity. Nat Neurosci 11:713-720.

Durst ME, Zhu G, Xu C (2006) Simultaneous spatial and temporal focusing for axial scanning. Opt Express 14:12243-12254.

Fan GY, Fujisaki H, Miyawaki A, Tsay RK, Tsien RY, Ellisman MH (1999) Video-rate scanning two-photon excitation fluorescence microscopy and ratio imaging with cameleons. Biophysical journal 76:2412-2420.

Fernandez-Alfonso T, Nadella KM, Iacaruso MF, Pichler B, Ros H, Kirkby PA, Silver RA (2014) Monitoring synaptic and neuronal activity in 3D with synthetic and genetic indicators using a compact acousto-optic lens two-photon microscope. J Neurosci Methods 222:69-81.

Gobel W, Kampa BM, Helmchen F (2007) Imaging cellular network dynamics in three dimensions using fast 3D laser scanning. Nat Methods 4:73-79.

Goeppert-Mayer M (1931) Ueber Elementarakte mit zwei Quantenspruengen. Ann Phys 9:273.

Golgi C (1873) Sulla struttura della sostanza grigia dell cervello. Gazz Med Lombarda 33:244-246.

Grewe BF, Helmchen F (2009) Optical probing of neuronal ensemble activity. Curr Opin Neurobiol 19:520-529.

Grewe BF, Voigt FF, van 't Hoff M, Helmchen F (2011) Fast two-layer two-photon imaging of neuronal cell populations using an electrically tunable lens. Biomedical optics express 2:2035-2046.

Grewe BF, Langer D, Kasper H, Kampa BM, Helmchen F (2010) High-speed in vivo calcium imaging reveals neuronal network activity with near-millisecond precision. Nat Methods 7:399-405.

Gross CG (1995) Aristotle on the Brain. The Neuroscientist 1:245-250.

Hafting T, Fyhn M, Molden S, Moser MB, Moser EI (2005) Microstructure of a spatial map in the entorhinal cortex. Nature 436:801-806.

Hajos N, Ellender TJ, Zemankovics R, Mann EO, Exley R, Cragg SJ, Freund TF, Paulsen O (2009) Maintaining network activity in submerged hippocampal slices: importance of oxygen supply. Eur J Neurosci 29:319-327.

Hell SW, Wichmann J (1994) Breaking the diffraction resolution limit by stimulated emission: stimulated-emission-depletion fluorescence microscopy. Opt Lett 19:780-782.

Helmchen F, Denk W (2005) Deep tissue two-photon microscopy. Nat Methods 2:932-940.

Holekamp TF, Turaga D, Holy TE (2008) Fast three-dimensional fluorescence imaging of activity in neural populations by objective-coupled planar illumination microscopy. Neuron 57:661-672.

Iyer V, Hoogland TM, Saggau P (2006) Fast functional imaging of single neurons using random-access multiphoton (RAMP) microscopy. J Neurophysiol 95:535-545.

Jia H, Rochefort NL, Chen X, Konnerth A (2010) Dendritic organization of sensory input to cortical neurons in vivo. Nature 464:1307-1312.

Johnston D, Narayanan R (2008) Active dendrites: colorful wings of the mysterious butterflies. Trends Neurosci 31:309-316.

Kaplan A, Friedman N, Davidson N (2001) Acousto-optic lens with very fast focus scanning. Opt Lett 26:1078-1080.

Kerr JN, Denk W (2008) Imaging in vivo: watching the brain in action. Nat Rev Neurosci 9:195-205.

Kherlopian AR, Song T, Duan Q, Neimark MA, Po MJ, Gohagan JK, Laine AF (2008) A review of imaging techniques for systems biology. BMC systems biology 2:74.

Kirkby PA, Srinivas Nadella KM, Silver RA (2010) A compact Acousto-Optic Lens for 2D and 3D femtosecond based 2-photon microscopy. Opt Express 18:13721-13745.

Kobat D, Horton NG, Xu C (2011) In vivo two-photon microscopy to 1.6-mm depth in mouse cortex. J Biomed Opt 16:106014.

Kovalchuk Y, Eilers J, Lisman J, Konnerth A (2000) NMDA receptor-mediated subthreshold Ca(2+) signals in spines of hippocampal neurons. J Neurosci 20:1791-1799.

Losonczy A, Makara JK, Magee JC (2008) Compartmentalized dendritic plasticity and input feature storage in neurons. Nature 452:436-441.

Magee JC, Johnston D (2005) Plasticity of dendritic function. Curr Opin Neurobiol 15:334-342.

Mainen ZF, Malinow R, Svoboda K (1999) Synaptic calcium transients in single spines indicate that NMDA receptors are not saturated. Nature 399:151-155.

Minsky M (1988) Memoir on inventing the confocal scanning microscope. Scanning 10:128-138.

Niesner R, Andresen V, Neumann J, Spiecker H, Gunzer M (2007) The power of single and multibeam two-photon microscopy for high-resolution and high-speed deep tissue and intravital imaging. Biophysical journal 93:2519-2529.

Nikolenko V, Watson BO, Araya R, Woodruff A, Peterka DS, Yuste R (2008) SLM Microscopy: Scanless Two-Photon Imaging and Photostimulation with Spatial Light Modulators. Front Neural Circuits 2:5.

Nimmerjahn A, Kirchhoff F, Kerr JN, Helmchen F (2004) Sulforhodamine 101 as a specific marker of astroglia in the neocortex in vivo. Nat Methods 1:31-37.

Ohki K, Chung S, Ch'ng YH, Kara P, Reid RC (2005) Functional imaging with cellular resolution reveals precise micro-architecture in visual cortex. Nature 433:597-603.

Otsu Y, Bormuth V, Wong J, Mathieu B, Dugue GP, Feltz A, Dieudonne S (2008) Optical monitoring of neuronal activity at high frame rate with a digital random-access multiphoton (RAMP) microscope. J Neurosci Methods 173:259-270.

Petráň M, Hadravský M, Egger MD, Galambos R (1968) Tandem-Scanning Reflected-Light Microscope. J Opt Soc Am 58:661-664.

Prevedel R, Yoon YG, Hoffmann M, Pak N, Wetzstein G, Kato S, Schrodel T, Raskar R, Zimmer M, Boyden ES, Vaziri A (2014) Simultaneous whole-animal 3D imaging of neuronal activity using light-field microscopy. Nat Methods 11:727-730.

Proctor B, Wise F (1992) Quartz prism sequence for reduction of cubic phase in a mode-locked Ti:Al(2)O(3) laser. Opt Lett 17:1295-1297.

Quirin S, Peterka DS, Yuste R (2013) Instantaneous three-dimensional sensing using spatial light modulator illumination with extended depth of field imaging. Opt Express 21:16007-16021.

Quirin S, Jackson J, Peterka DS, Yuste R (2014) Simultaneous imaging of neural activity in three dimensions. Front Neural Circuits 8:29.

Reddy GD, Saggau P (2005) Fast three-dimensional laser scanning scheme using acousto-optic deflectors. J Biomed Opt 10:064038.

Rozsa B, Zelles T, Vizi ES, Lendvai B (2004) Distance-dependent scaling of calcium transients evoked by backpropagating spikes and synaptic activity in dendrites of hippocampal interneurons. J Neurosci 24:661-670.

Salome R, Kremer Y, Dieudonne S, Leger JF, Krichevsky O, Wyart C, Chatenay D, Bourdieu L (2006) Ultrafast random-access scanning in two-photon microscopy using acousto-optic deflectors. J Neurosci Methods 154:161-174.

Schiller J, Major G, Koester HJ, Schiller Y (2000) NMDA spikes in basal dendrites of cortical pyramidal neurons. Nature 404:285-289.

Spruston N (2008) Pyramidal neurons: dendritic structure and synaptic integration. Nat Rev Neurosci 9:206-221.

DOI:10.15774/PPKE.ITK.2015.003

Stosiek C, Garaschuk O, Holthoff K, Konnerth A (2003) In vivo two-photon calcium imaging of neuronal networks. Proc Natl Acad Sci U S A 100:7319-7324.

Theer P, Hasan MT, Denk W (2003) Two-photon imaging to a depth of 1000 microm in living brains by use of a Ti:Al2O3 regenerative amplifier. Opt Lett 28:1022-1024.

Tomer R, Khairy K, Amat F, Keller PJ (2012) Quantitative high-speed imaging of entire developing embryos with simultaneous multiview light-sheet microscopy. Nat Methods 9:755-763.

Veress M, Barocsi A, Richter P, Maak P (2010) Theoretical and experimental analyses of the acoustic-to-optic phase transfer in specific acousto-optic devices. Appl Opt 49:6-11.

Vucinic D, Sejnowski TJ (2007) A compact multiphoton 3D imaging system for recording fast neuronal activity. PLoS One 2:e699.

Yuste R, Majewska A, Holthoff K (2000) From form to function: calcium compartmentalization in dendritic spines. Nat Neurosci 3:653-659.